8-1-1992

Modeling of a-Si : H deposition in a DC glow discharge reactor

Dariusz Orlicki
Laboratory for ceramic and reaction engineering, Department of chemical engineering, State University of New York at Buffalo, New York, 14260.

Vladimir Hlavacek
Laboratory for ceramic and Reaction Engineering, Department of chemical Engineering, State University of New York at Buffalo, New York.

Hendrik J. Viljoen
University of Nebraska-Lincoln, hviljoen1@unl.edu

Modeling of a–Si:H deposition in a dc glow discharge reactor

Dariusz Orlicki and Vladimir Hlavacek
Laboratory for Ceramic and Reaction Engineering, Department of Chemical Engineering, State University of New York at Buffalo, Buffalo, New York 14260

Hendrik J. Viljoen[a)]
Department of Chemical Engineering, University of Nebraska–Lincoln, Lincoln, Nebraska 68588–0126

(Received 16 July 1991; accepted 17 April 1992)

PECVD reactors are increasingly used for the manufacturing of electronic components. This paper presents a reactor model for the deposition of amorphous hydrogenated silicon in a dc glow discharge of $Ar–SiH_4$. The parallel-plate configuration is used in this study. Electron and positive ion densities have been calculated in a self-consistent way. A macroscopic description that is based on the Boltzmann equation with forwardscattering is used to calculate the ionization rate. The dissociation rate constant of SiH_4 requires knowledge about the electron energy distribution function. Maxwell and Druyvesteyn distributions are compared and the numerical results show that the deposition rate is lower for the Druyvesteyn distribution. The plasma chemistry model includes silane, silyl, silylene, disilane, hydrogen, and atomic hydrogen. The sensitivity of the deposition rate toward the branching ratios SiH_3 and SiH_2 as well as H_2 and H during silyl dissociation is examined. Further parameters that are considered in the sensitivity analysis include anode/cathode temperatures, pressure, applied voltage, gap distance, gap length, molar fraction of SiH_4, and flow speed. This work offers insight into the effects of all design and control variables.

I. INTRODUCTION

Plasma enhanced CVD (PECVD) has gained prominence as an important material processing tool since its introduction in the mid 60's. In the PECVD process, gases are ionized by an electric energy source to form a plasma. Through the intermediation of the highly energized electrons, radical species are formed from the precursor molecular gases. These radicals are chemically very active, and their stability in the gas phase is determined by the rate of recombination and disproportionation reactions. The more stable radicals diffuse to the reactor walls where they are depleted by rapid insertion reactions. One outstanding feature of the PECVD process is the ability to energize electrons to very high levels, without any significant rise in the gas temperature. Processing at lower substrate temperature holds several advantages; e.g., temperature-sensitive material can be used, and a reduction in residual stress results, due to thermal mismatch.

Whereas traditional CVD systems employed thermal energy to assist the deposition reaction, PECVD uses electrons produced by the glow discharge. The advantages of PECVD are obvious, but the understanding of and the ability to control this system are considerably more complex than thermal CVD processes. Historically, PECVD was developed for microelectronic applications. Passivation layers, diffusion masks, and interlayer dielectrics can be deposited at low temperatures. But the major advantage of PECVD was realized when macroelectronic devices were fabricated by this method. Examples are photovoltaic cells, large area display panels, linear arrays, and other thin film based technology.

Recently PECVD was used to deposit thin films of polycrystalline diamond.[1] Microwave plasmas are normally used for diamond deposition, but they have certain limitations. If a PECVD process can be devised that produces a large concentration of atomic hydrogen and sufficient ion bombardment to remove any pyrolytic carbon, it has a good chance to deposit diamond-like film at a fast rate. This brings us to the philosophy of a generic reactor design. Different objectives will lead to different designs. For example, if it is desirable to have a large concentration of atomic hydrogen, gap space and electric field strength are the crucial factors; if a uniform deposition rate is the objective, then the hydrodynamic design will require more attention and in industrial reactors, conversion and yield are the decisive factors in the design process.

The glow discharge decomposition of silane to produce amorphous hydrogenated silicon (a–Si:H) is the most well-known PECVD process. It is important because of its use in solar cells and thin film transistors.[2] The Japanese have also embarked on a program to scale-up plasma processes to achieve time and cost reduction in device fabrication through mass production.

[a)]Author to whom correspondence should be addressed.

In particular, their 'Sunshine Project'[3] is aimed at the development of low-cost mass production techniques for fabricating a–Si:H solar cells. Another crucial development was the discovery in 1975 that the electronic properties of the glow discharge deposited material could be controlled very effectively by substitutional doping from the gas phase.[4] This possibility has opened a rapidly growing new field of research and applications.

The motivation for this work is to develop an integrated model that can be used to predict film growth rate and uniformity and analyze the sensitivity of these qualities. The model finds important applications in the design, scale-up, and characterization of PECVD reactors. The model consists of two parts; the first part models the glow discharge and the second part describes the plasma chemistry and the spatial distribution of the neutral species.

A macroscopic approach was followed to derive the model for the glow discharge. This implies that electron and ion behavior are described by a one-dimensional continuum model and the rate of ionization is determined by a nonequilibrium, macroscopic relation with the electric field. The electron and ion density distributions, the electric field, and the rate of ionization then give a self-consistent description of the glow discharge and these equations are solved numerically. Space discretization was done according to the Scharfetter–Gummel scheme. Starting from an estimated solution, it was improved by implicit integration of a false transient form of the equations. The steady state solution was then calculated by Newton's method.

For the second part of the model, a two-dimensional compressible fluid flow model was used to calculate the concentration of all neutral species, and the ideal gas law was used as the equation of state. A Galerkin finite element method was used to calculate the velocity, temperature, and concentration fields, and the deposition rates and profiles along the electrode surfaces were also calculated. The model also made provision for the temperature and pressure dependencies of all the physical properties. Special consideration was given to the physical properties of the atomic hydrogen and the radicals. But the keystone of the process is, of course, the electron-silane dissociation reactions, and little will be gained by paying attention to the other details while neglecting this step.

The dissociation of silane produces silyl and silylene. But the formation of silylene also occurs along two possible routes; in one case hydrogen is produced and in the other case molecular hydrogen is produced. Distinction between these two routes is important since atomic hydrogen participates in a secondary hydrogen extraction reaction with silane to form silyl. The experimental collision cross section for dissociation does not distinguish among the different dissociation reactions, and branching among the three possible reactions introduces two additional parameters to the system. The rate of dissociation warrants some discussion, since it plays such an important role. The main disadvantage of any macroscopic approach is the lack of information about the electron energy distribution (EEDF). The EEDF is required to calculate the dissociation rate. In this study we will assume two forms of the EEDF, namely the Maxwellian and the Druyvesteyn distributions. The mechanism of film growth is not perfectly clear, but it is known (cf. Kushner[5]) that silylene can insert directly into saturated silicon bonds on the surface, while silyl can insert only into a dangling bond (i.e., $\equiv Si - \cdot$). The emission of hydrogen from the film underlies the insertion rates, but in this model sticking coefficients of unity were used for both silyl and silylene.

Deposition rates and profiles on both electrodes are calculated and compared for the different energy distributions. Furthermore, a parameter study was done where the values of all the parameters of the model were varied by $\pm 10\%$ from a base case and changes in deposition rates and film uniformity were used to rank the sensitivity of all the parameters.

II. THE MODEL

A model that describes the behavior of a PECVD reactor consists of the conservation equations for charge, mass, energy, and momentum as well as the transport of charged and chemically active species. In this model a feeding gas of Ar and SiH_4, where the silane concentration is in the order of 1%, is considered. The addition of a molecular gas to the noble gas will affect the electron energy distribution. But we considered only the ionization of Ar in the model; since silane is not included in the glow discharge model, the chemistry/hydrodynamic part of the model becomes decoupled from the discharge with significant savings in computing times. To make this assumption more justifiable, we considered only mole fractions of silane in the range of 1%.

A. Glow discharge

A continuum description for the behavior of the glow discharge is followed. The continuum description is valid only as long as certain criteria are met. The most important one is that the number of charged particles contained in a sphere of Debye radius is large.

$$n \times \frac{4}{3}\pi l_D^3 = n_D \gg 1 \tag{1}$$

$$l_D = \left(\frac{\epsilon_0 k_B T}{\rho_c e}\right)^{1/2} \tag{2}$$

where ϵ_0 is the permittivity of free space, k_B is the Boltzmann constant, ρ_c is the charge density, and e

is the charge of a particle. This condition limits the plasma charge granularity and ensures weak potential interactions.

Since Ar is an electropositive gas, the model will not include any anion formation; i.e., any inelastic collision between an electron and an Ar-atom will have a negligible probability to be of the associative type. The governing equations for the glow discharge are as follows.

1. Electron conservation equation

$$\frac{\partial n_e}{\partial t} + \nabla \cdot j_e = \alpha j_e \frac{N}{N_0} \tag{3}$$

This balance for the electron density n_e considers only electron-neutral impact ionization as a source term; due to the low degree of ionization the change in Ar-concentration is very small and N/N_0 remains close to unity. Hence the glow discharge is decoupled from any neutral species balance.

2. Positive ion conservation equation

$$\frac{\partial n_p}{\partial t} + \nabla \cdot j_p = \alpha j_e \tag{4}$$

The fluxes j_e and j_p are defined for the potential V as

$$j_e = -D_e \nabla n_e + \mu_e n_e \nabla V \tag{5}$$

$$j_p = -D_p \nabla n_p - \mu_p n_p \nabla V \tag{6}$$

First it should be noted that the term for convective transport tacitly implies a momentum balance for the charged species of the form

$$e_k E + \nu_{km} m U_k = 0, \qquad k = e, p \tag{7}$$

where U_k is the velocity and in e_k the sign of the charge should be taken into consideration. The mobility μ_k can be easily inferred from Eq. (7). ν_{km} is a collision frequency for momentum transfer. Experimental values for mobilities and diffusion coefficients will be used in this model (see Appendix). The potential in the gap is given by the Poisson equation.

3. Poisson equation

$$\nabla^2 V = -\frac{|e|}{\epsilon_0}(n_p - n_e) \tag{8}$$

The ionization coefficient α determines the rate of electron generation, and either a microscopic or a macroscopic approach can be followed. If the microscopic approach is followed, all swarm parameters, including α, are determined by solving the Boltzmann equation. A less arduous approach is to determine α by a macroscopic approach. One possibility is to ascribe to the electrons a certain energy distribution (EEDF), e.g., a Maxwellian distribution, then the concept of electron temperature can be introduced and ionization is treated as in chemical reaction theory. Graves and Jensen[6] used this method and assumed a kinetic form of the Arrhenius-type. Segur *et al.*[7] defined a memory kernel for their nonequilibrium model and fitted it to values for a He-plasma. Friedland[8,9] derived a nonequilibrium model, based on the forwardscattering form of the Boltzmann equation; i.e., the distribution function depends only on one spatial dimension and energy. Taking the first and second moments of the Boltzmann equation (with respect to energy) and using the assumptions that the ionization and excitation cross sections depend linearly on energy ($Q_i = a\epsilon, Q_e = k\epsilon$), the following equation is found for α:

$$\frac{d\alpha}{dz} + \alpha^2 + pk\xi\alpha - paE = 0 \tag{9}$$

where k and a are the coefficients of the excitation and ionization cross sections, respectively, and p is the total pressure. ξ is the amount of energy that is lost by an electron in a collision and it is taken as the mean of the excitation and ionization values:

$$\xi = \frac{1}{2}(\xi_{ion} + \xi_{exc}) \tag{10}$$

The energy loss for excitation collisions (ξ_{exc}) also presents an average of the different excitation collisions that are possible.[10] The ionization rate is highest in the cathodic sheath region, and in this region the assumptions of the Friedland formulation hold best. Although the assumptions are no longer valid in the bulk plasma, the ionization is low and the error will not affect the model qualitatively. To improve the model will require a self-consistent microscopic description, but at the expense of excessive computing times.

There exists quite a variety of reactor configurations; the most popular are the parallel-plate type and the concentric cylinders with axial flow. The configuration that will be used in our model is a parallel-plate reactor, shown schematically in Fig. 1. Inlet and outlet sections are provided for flow stabilization. Based on this configuration, we will also assume that the charge species will have only unidirectional motion, and any axial advection will be negligible compared to the electric-field directed motion. Hence the Laplace and del-operators can be written as second and first derivatives with respect to z.

The boundary conditions used in the calculations are as follows:

The cathode $(-H/2)$ is not transparent for the flux of positive ions and the flux of electrons is due to secondary emission.

$$\left.\begin{aligned} j_e &= -\gamma j_p \\ \frac{dn_p}{dz} &= 0 \\ V &= -V_{DC} \end{aligned}\right\} z = -\frac{H}{2} \tag{11}$$

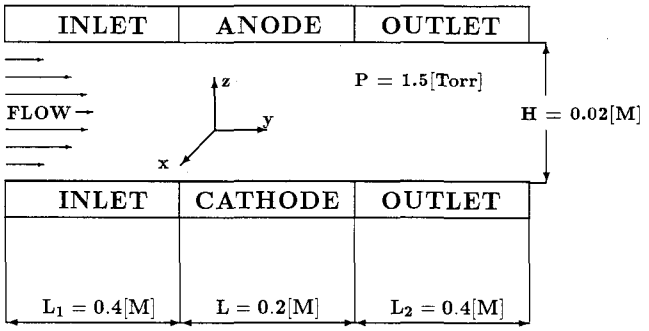

FIG. 1. Parallel-plate reactor schema.

where γ is the secondary emission coefficient.

The anode $(H/2)$ perfectly absorbs electrons and the flux of positive charged particles is set to zero.

$$\left.\begin{aligned} \frac{dn_p}{dz} &= 0 \\ n_e &= 0 \\ V &= 0 \end{aligned}\right\} z = \frac{H}{2} \tag{12}$$

B. Hydrodynamic model of reactor

Gas flows through the reactor and the transport of neutral species are not affected by the electric field. The ionization in typical glow discharges accounts for a conversion of only one part per million and therefore the neutral species mass balances and momentum balances are decoupled from the rest of the plasma model. In order to describe the distribution and fluxes of neutral species, specifically the silane and radicals, a two-dimensional compressible flow model is used.

1. Continuity equation

$$\nabla \cdot (\rho \mathbf{U}) = 0 \tag{13}$$

2. Momentum equations

$$\rho \frac{D\mathbf{U}}{Dt} = -\nabla \mathbf{p} - \nabla \cdot \bar{\tau} + p\mathbf{g} \tag{14}$$

where D/Dt denotes the substantial derivative and ∇ represents the divergence operator. The viscous tensor $\bar{\tau}$ is defined for a Newtonian fluid as

$$\bar{\tau} = -\mu\left(\nabla \mathbf{U} + (\nabla \mathbf{U})^{\mathrm{T}}\right) + \frac{2}{3}\mu \nabla \cdot \mathbf{U}\mathbf{I} \tag{15}$$

In the energy conservation equation, the effects due to changes in pressure, viscous dissipation, and concentration gradients (Dufour effect) were neglected.

3. Energy equation

$$\rho C_p \frac{DT}{Dt} = \nabla \cdot \mathbf{k} \nabla T \tag{16}$$

The system is closed by an equation of state, and for our operating conditions the ideal gas law was used.

4. Equation of state

$$R_g T \rho = p \sum_{i=1}^{n} M_i x_i \tag{17}$$

If the average molecular mass of the gas is assumed to be constant, the conservation equation for any species can be written as

5. Conservation of mass

$$C\frac{Dx_i}{Dt} = \nabla \cdot [CD_i(\nabla \mathrm{x_i} + \alpha_i \mathrm{x_i} \nabla \ln \mathbf{T})] + \mathbf{R}\left(\sum_{\mathrm{j}} \mathrm{x_j}\right) \tag{18}$$

The choice of boundary conditions is also a point of contention, and these conditions must be chosen in such a way that they correctly describe the prevalent physical conditions at any boundary. The configuration that is used has fore- and after-section with the electrodes in between. The flow is then developed when it enters the fore-section and Poiseuille flow also prevails at the end of the after-section;

$$\mathbf{U} = (0, U_p, 0) \tag{19}$$

where U_p denotes the Poiseuille solution. At solid walls the non-slip condition was applied

$$\bar{\mathbf{n}} \cdot \mathbf{U} = 0 \tag{20}$$

$$\bar{\mathbf{t}} \cdot \mathbf{U} = 0 \tag{21}$$

where $\bar{\mathbf{n}}$ and $\bar{\mathbf{t}}$ denote unit normal and tangential vectors to the solid walls. For the temperature and mass balance equations, the Danckwerts boundary conditions are used. At the inlet of the reactor

$$\bar{\mathbf{n}} \cdot \mathbf{U} \rho C_p (T - T_0) = \mathbf{k}\, \bar{\mathbf{n}} \cdot \nabla \mathbf{T} \tag{22}$$

$$\bar{\mathbf{n}} \cdot \mathbf{U}(x_i - x_{i,0}) = D_i(\bar{\mathbf{n}} \cdot \nabla x_i + \alpha_i x_i \bar{\mathbf{n}} \cdot \nabla \ln T) \tag{23}$$

and at the outlet of the reactor section

$$\bar{\mathbf{n}} \cdot \nabla T = 0 \tag{24}$$

$$\bar{\mathbf{n}} \cdot \nabla x_i + \alpha_i x_i \bar{\mathbf{n}} \cdot \nabla \ln T = 0 \tag{25}$$

The surface on the upper part of the reactor system, which includes the fore-section, anode, and after-section, is kept at a constant temperature

$$T\left(z = \frac{H}{2}\right) = T_{an} \tag{26}$$

but the temperature on the bottom part is ramped linearly from T_{an} in the fore-section to T_{cat} at the beginning of the cathode, and is linearly decreased in the after-section down to T_{an}.

C. Nondimensionalization

The model discussed in the previous sections is made nondimensional by using a set of scales. The height H between the electrodes is used to scale vertical distance, the length of the electrodes is used for scaling axial distance, and the applied voltage at the cathode is used for scaling potential.

An arbitrary number density n_0 is used to scale particle densities of the charged species. Neutral species are expressed as a mole fraction. The pressure and temperature at inlet stream are chosen to scale physical properties of gaseous species, which are used to define all dimensionless groups. Velocity is scaled by the ratio, $v_{ref} = g(0.5H)^2/\nu$, pressure is scaled by $\mu_{ref}v_{ref}/(H/2)$, and dimensionless temperature θ is defined as T/T_{ref}. The definitions of all the dimensionless parameters are shown in the Table I. Note that notation has not been changed from the dimensionless formulation.

The model of a dc glow discharge now takes the form

$$Fo_e\frac{dn_e}{dt} + \frac{dj_e}{dz} = \alpha j_e \tag{27}$$

$$Fo_p\frac{dn_p}{dt} + \frac{dj_p}{dz} = \beta\alpha j_e \tag{28}$$

$$\frac{d^2V}{dz^2} = -b(n_p - n_e) \tag{29}$$

where the dimensionless fluxes j_e and j_p are

$$j_e = -\frac{dn_e}{dz} + Pe_e n_e\frac{dV}{dz} \tag{30}$$

$$j_p = -\frac{dn_p}{dz} - Pe_p n_p\frac{dV}{dz} \tag{31}$$

TABLE I. Definitions of parameters and typical values.

Parameter	Definition	Value
β	$\frac{D_e}{D_p}$	$2.3\cdot10^4$
τ	$\min\left(\frac{(0.5H)^2}{D_i}, \frac{(0.5H)^2}{\mu_i V_{DC}}\right); i = e, p$	$5.12\cdot10^{-9}$ (s)
Pe_e	$\frac{\mu_e V_{DC}}{D_e}$	$1.71\cdot10^2$
Pe_p	$\frac{\mu_p V_{DC}}{D_p}$	$1.14\cdot10^4$
Fo_e	$\frac{(0.5H)^2}{D_e\tau}$	$1.71\cdot10^2$
Fo_p	$\frac{(0.5H)^2}{D_p\tau}$	$4.00\cdot10^6$
δ	$pk\xi(0.5H)$	5.22
ϵ	$paV_{DC}(0.5H)$	$1.48\cdot10^2$
b	$\frac{n_0(0.5H)^2\lvert e\rvert}{V_{DC}\epsilon_0}$	12.06
Gr	$\frac{\rho_{ref}^2(0.5H)^3 g}{\mu_{ref}^2}$	$3.12\cdot10^{-2}$
Ra	$Gr\frac{\mu_{ref}Cp_{ref}}{k_{ref}}$	$2.21\cdot10^{-2}$
Pe_{SiH_4}	$\frac{(0.5H)^3 g\rho_{ref}}{\mu_{ref}D_{ref}}$	$2.68\cdot10^{-2}$
k_4	Reaction constant Eq.(47)	$5.0\cdot10^{-18}$ ($m^3\cdot s^{-1}$)
k_5	Reaction constant Eq.(48)	$1.0\cdot10^{-16}$ ($m^3\cdot s^{-1}$)
k_6	Reaction constant Eq.(49)	$1.7\cdot10^{-17}$ ($m^3\cdot s^{-1}$)

The Friedland equation is written as:

$$\frac{d\alpha}{dz} + \alpha^2 + \delta\alpha - \epsilon\frac{dV}{dz} = 0 \tag{32}$$

1. Continuity equation

$$\nabla\cdot\left(\frac{U}{\Theta}\right) = 0 \tag{33}$$

2. Momentum equations

$$\frac{Gr}{\Theta}\left(u_y\frac{\partial u_y}{\partial y} + u_z\frac{\partial u_y}{\partial z}\right)\left(\frac{L}{H}\right) = -\left(\frac{H}{L}\right)\frac{\partial p}{\partial y} - \left(\frac{H}{L}\right)\frac{\partial\tau_{yy}}{\partial y} - \frac{\partial\tau_{yz}}{\partial z} \tag{34}$$

$$\left(\frac{Gr}{\Theta}\right)\left(u_y\frac{\partial u_z}{\partial z} + u_z\frac{\partial u_z}{\partial z}\right) = -\frac{\partial p}{\partial z} - \frac{\partial\tau_{zz}}{\partial z} - \left(\frac{H}{L}\right)\frac{\partial\tau_{yz}}{\partial y} + \frac{1}{\Theta} \tag{35}$$

where

$$\tau_{yy} = -\left(\frac{\mu}{\mu_{ref}}\right)\left(\frac{2}{3}\right)\left(2\frac{\partial u_y}{\partial y} - \frac{\partial u_z}{\partial z}\right) \tag{36}$$

$$\tau_{zz} = -\left(\frac{\mu}{\mu_{ref}}\right)\left(\frac{2}{3}\right)\left(2\frac{\partial u_z}{\partial z} - \frac{\partial u_y}{\partial y}\right) \tag{37}$$

$$\tau_{yz} = -\left(\frac{\mu}{\mu_{ref}}\right)\left[\left(\frac{H}{L}\right)\frac{\partial u_z}{\partial y} + \left(\frac{L}{H}\right)\frac{\partial u_y}{\partial z}\right] \tag{38}$$

3. Energy equation

$$\left(\frac{Ra}{\Theta}\right)\left(\frac{Cp}{Cp_{ref}}\right)\left(u_y\frac{\partial\Theta}{\partial y} + u_z\frac{\partial\Theta}{\partial z}\right) = \left(\frac{k}{k_{ref}}\right)\left[\left(\frac{H}{L}\right)^2\frac{\partial^2\Theta}{\partial y^2} + \frac{\partial^2\Theta}{\partial z^2}\right] \tag{39}$$

4. Concentration equation

$$\left(\frac{Pe_{im}}{\Theta}\right)\left(u_y\frac{\partial x_i}{\partial y} + u_z\frac{\partial x_i}{\partial z}\right) = \frac{\partial}{\partial y}\left(\frac{D_i}{D_{ref}\Theta}\left(\frac{\partial x_i}{\partial y} + \frac{\alpha_i x_i}{\Theta}\frac{\partial\Theta}{\partial y}\right)\right) + \left(\frac{H}{L}\right)^2\frac{\partial}{\partial z}\left(\frac{D_i}{D_{ref}\Theta}\left(\frac{\partial x_i}{\partial z} + \frac{\alpha_i x_i}{\Theta}\frac{\partial\Theta}{\partial z}\right)\right) \pm Daf\left(\sum_j x_j\right) \tag{40}$$

III. NUMERICAL METHOD

Based on our assumptions, the solving procedure has been divided into two parts: the glow discharge and the hydrodynamic description of the reactor. Both are coupled through the reaction between electrons and silane. Other interactions between plasma field and gas flow in the reactor are not taken into consideration.

A. Glow discharge

Due to high nonlinearity and strong coupling of the governing equations, the treatment of these equations poses a difficult numerical problem. Examples of a few attempts to solve this problem can be found in the literature.

1. Ward[11] pioneered numerical modeling of glow discharges. He used a shooting technique to solve the equations.

2. Lowke and Davies[12] used an explicit relaxation method and obtained the steady state from the dynamic form of the equations; a predictor-corrector method was used for time integration.

3. Graves and Jensen[6] solved both the dc and rf problem. The latter problem was considered as a boundary value problem in the time domain, and a Fourier expansion was used to present time variations.

4. Kushner[13] discretized spatial functions by finite differences and integrated the equations in time by a third order Runge–Kutta.

5. Boeuf[14] adapted the implicit exponential scheme of Scharfetter and Gummel to model a two-dimensional dc glow discharge.

The problem of electron and hole transport in semiconductor devices is analogous to the glow discharge problem.

6. Traar *et al.*[15] discussed a wide range of iteration methods for these types of convective dominant transport equations.

The implicit exponential scheme of Scharfetter and Gummel[14] has been chosen to discretize the continuity equations. The main advantage of this scheme is its robustness, stability, and ability to deal with situations where either the convection or diffusion component of the total flux is dominant (these situations correspond, respectively, to the sheath and plasma regions).

The source term in the continuity equation is implemented into a computer code as a continuous and smooth function of ionization coefficient α, and electron flux j_e:

$$r_i = \left(\frac{1}{2} + \frac{1}{\pi}\tan^{-1}(s * \alpha)\right)\alpha|j_e| \qquad (41)$$

and s is a parameter chosen arbitrarily large.

The symmetric finite difference approximation is used for the Poisson equation. Friedland's equation is discretized by backward finite difference. Physical domain (cathode = 0, anode = H) is mapped onto a computational domain (interval $x \in [-1, 1]$). In our calculation an equidistant mesh is used.

After discretizing in the space domain, an initial value problem is obtained which is integrated by a second-order accurate trapezoid rule. The Newton–Raphson iterative scheme is used to obtain the solution at each step and finally to find steady-state solution when the time derivatives diminish. The discretization of governing equations has resulted in the set of nonlinear algebraic-equations

$$\Omega(y) = 0 \qquad (42)$$

where the vector of unknowns is represented as

$$y = (n_{e4i-3}, V_{4i-2}, n_{p4i-1}, \alpha_{4i}, \ldots) \qquad i = 1, 2, \ldots N_t \qquad (43)$$

N_t: total number of nodes in the computational domain.

Since matrix Ω is sparse, the advantage of its band-matrix representation is used for calculations. Each step in the Newton–Raphson method requires the solution of the linear system. In the numerical routine LU-decomposition has been used. At each step (starting from $i \geq 2$) the ratio $\|\delta_{i-1}\|_\infty / \|\delta_i\|_\infty$ is checked for convergence against the specified number and only if this ratio becomes smaller than 100, the Jacobian is updated; otherwise the LU-decomposition from the previous step is used. The electric field and ionization term are updated only once at each time step.

During marching in time the size of the time step depends upon deviation from steady state solution. The strategy for varying the step size Δt_n is based on estimation of the local truncation error.[16]

B. Numerical solution of hydrodynamic model

The partial differential equations conserving momentum, heat, and mass transfer are numerically solved by the Galerkin finite element method. The code was developed to handle both diffusion and advection-dominated problems. In order to overcome oscillations in the latter case, artificial dispersion is introduced.[17]

In applying the Galerkin finite element method to the hydrodynamic model, pressure has to be approximated with trial functions of one order lower than the trial functions for velocity, temperature, and concentration. The artificial dispersion is introduced into the momentum equations in a form that is referred to as the streamline upwind method (SU)[17] and into the energy and concentration balances by the SU Petrov–Galerkin method (see Brooks and Hughes[18]). Finally, the system of nonlinear algebraic equations is solved by the Newton–Raphson method. To improve the initial guess, a false transient method is adopted.

IV. RATE OF SILANE DISSOCIATION

Although the glow discharge deposition of silane to produce a–Si:H is the most studied plasma enhanced CVD process, the details of the silane plasma chemistry are still debated. Controversy exists over the dominance of the silylene or silyl radicals in the deposition process.[5,19]

In pure amorphous silicon, atoms that are only threefold coordinated have an unpaired electron, referred to as a dangling bond. These unpaired electrons impair the film's photoconductivity and photoluminescence. In hydrogenated amorphous silicon the density of dangling bonds is greatly reduced, because hydrogen can bond to single silicon atoms. Not all hydrogen incorporated in the silicon structure attaches to dangling bonds; it is reported by Thomas[20] that hydrogen preferentially diffused into a hydrogen-rich phase that was interdispersed between a columnar phase of monohydride Si–H groups. Only hydrogen that is incorporated in the latter phase will lead to a reduction in the dangling bond density. In a weakly ionized glow, neutral radical species in the ground electronic state play important roles in depositing a–Si:H; they directly participate in the chemical and physical processes on the surface of the deposit.

Plasma chemistry

Electron collisions with silane produce a wide range of products, but the majority of these products are not stable. The major branching processes for neutral dissociation are:

$$e + SiH_4 \xrightarrow{k_1} SiH_3 + H + e \quad (44)$$

$$\xrightarrow{k_2} SiH_2 + H + H + e \quad (45)$$

$$\xrightarrow{k_3} SiH_2 + H_2 + e \quad (46)$$

We define the following branching ratios:

$$\alpha = \frac{k_1}{k_1 + k_2 + k_3}$$

$$\beta = \frac{k_2}{k_1 + k_2 + k_3}$$

Generation of H atoms during electron impact dissociation effectively increases the rate of production of radicals due to the following reaction:

$$H + SiH_4 \xrightarrow{k_4} SiH_3 + H_2 \quad (47)$$

Silylene is depleted by an insertion reaction with silane

$$SiH_2 + SiH_4 \xrightarrow{\kappa_=} Si_2H_6 \quad (48)$$

The insertion reaction is potentially fast and it produces disilane, which does not incorporate into the growing film. The silyl radical is more stable than the silylene radical and participates in few depleting reactions. The most important of these is a recombination reaction:

$$SiH_3 + SiH_3 \xrightarrow{k_6} SiH_2 + SiH_4 \quad (49)$$

Kushner[5] undertook a detail modeling of the silane dissociation chemistry in a glow discharge. He used maximum and minimum values for the rate constants of Eq. (48) and (49) which were available in literature. It was also found that the deposition rate is most sensitive to the yield of H atoms from the dissociation to SiH_2. Silyl is the only main contributor to film growth when the sticking coefficient exceeds 0.5. Along the guidelines provided by Kushner,[5] the rate constants for reactions (47)–(49) are listed in Table I.

Itabashi[21] *et al.* measured (and apparently the first time to do so) the spatial distribution of silyl radicals in an rf silane plasma, using infrared diode laser absorption spectroscopy. They used the following rate of deposition expression:

$$R_d = \Gamma \times S \times \frac{m}{p} \quad (50)$$

$$\Gamma = \frac{D_e}{\rho \times \beta} \frac{d(SiH_3)}{dx} \quad (51)$$

The loss probability $\beta \approx 0.26$, the sticking coefficient $S = 0.09$, which is quite a low value compared to the threshold value of Kushner,[5] $m = 4.7 \times 10^{-23}$ g, and $\rho = 2.21$ g/cm^3. They calculated $R_d = 0.40$ μm/h for a SiH_4/H_2 plasma at 80 mTorr and 125 W power deposition between a 3 cm gap. The experimental rate was 0.64 μm/h. To distinguish properly between silyl and silylene, their respective collision cross sections are required; unfortunately only global cross sections are available. Perrin *et al.*[22] measured global cross sections for dissociation of methane and silane for electron energies between 8 and 110 eV. The former value is the experimentally found threshold energy for dissociation of silane. Vicek[10] used explicit forms of cross sections for Ar, and we used their functional form to fit Perrin's experimental results.

$$\sigma_D = (7.1638 \times 10^{-10})^2 \frac{\left(\frac{\epsilon}{8} - 1\right)}{\left(\frac{\epsilon}{8}\right)^2} \ln\left(1.04315 \times \frac{\epsilon}{8}\right) \quad (52)$$

This curve fits the measured range of electron energy very well, and we used it to evaluate the cross section for the dissociation kinetics. To find the rate constant for dissociation, one requires knowledge of the electron

energy distribution function (EEDF):

$$k_D = \int_8^\infty \left(\frac{2\epsilon}{m}\right)^{0.5} f(\bar{\epsilon}, \epsilon)\sigma_D(\epsilon)\, d\epsilon \qquad (53)$$

where $\bar{\epsilon}(x)$ denotes an average electron energy at x.

The mean electron energy will be determined for the plasma, using the Friedland equation to model ionization. In Fig. 2 normalized values of the mean electron energy and the dissociation rate constants are shown. A sharp increase in energy in the sheath region is followed by a decline to a low energy in the remainder of the plasma. The maximum energy for this example (i.e., 600 V over a 2 cm gap) is 110 eV. One should not mistakenly attribute the decline in mean energy to collision processes. The main reason for the decrease in mean energy is the formation of an avalanche of new electrons, which gain far less energy than sheath electrons, and the mean is shifted toward this bulk of low-energy electrons. Information on the sheath electrons is lost. Another important factor that we want to point out is the contribution of electrons formed in the sheath to the total flux of electrons. Although the sheath electrons form a small fraction of the total electron number density, they form a significant fraction of the total electron flux. Therefore they make an important contribution to the production of radical species.

The Maxwell distribution gives the highest k_D value locally, but the values decrease sharply away from this point. The Druyvesteyn distribution gives a similar profile, but the values for k_D are smaller. The relation between reaction rate and mean energy is also evident from Fig. 2 and one can immediately see that most of the radical production will take place near the cathode. This conclusion is confirmed by the model of Yamaguchi

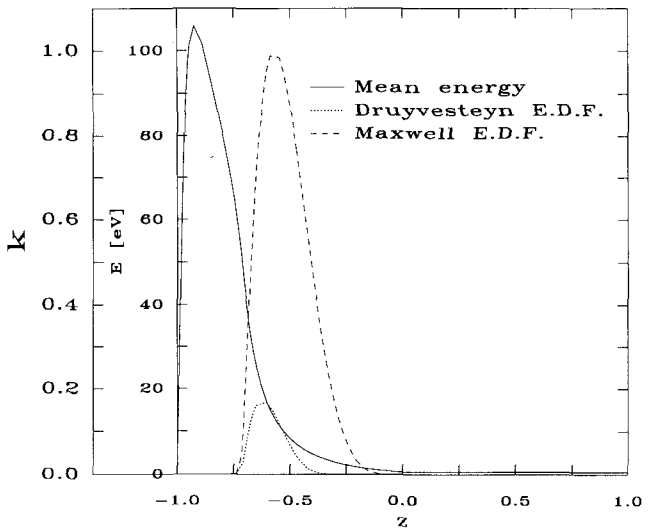

FIG. 2. Space evolution of electrons mean energy. Space evolution of reaction rate for Maxwell and Druyvesteyn electron energy distribution functions.

et al.[23] where it was found that the silyl concentration reaches a maximum in a small region near the cathode. They used dissociation collision frequencies R_d which were published by Ohmori *et al.*[24]

V. RESULTS

In this section the results of the plasma reactor model will be reported. But first a brief exposition of this section will be helpful. We start off by defining a scalar norm of the uniformity of deposition to measure reactor performance as a function of different parameters. Some results of the glow discharge itself are presented. Charged species concentrations, potential, and ionization rates are shown for a range of applied voltages, distances across the gap, and the total pressure.

For the sake of comparison, a base case is defined. The concentration fields of all species are shown for the base case. Next we do a sensitivity analysis. All the design and control variables are changed by ±10% from their base values and the change in the norm is calculated. Deposition rate profiles along the gap are shown for these different parameter values, including a comparison between the Maxwell and Druyvesteyn distributions. The effects of branching ratios (silane dissociation) on the deposition rate profiles are also presented.

It is not easy to define an unambiguous norm for a reactor. Solid state physical requirements of the film will most likely dictate different criteria. However, we will assume that only two factors determine the performance of the reactor: the rate of deposition and the uniformity of deposition. The first consideration is bounded from below by economical factors and from above by physical factors (e.g., particle formation, film quality, etc.). We will report average deposition rates on both electrodes, and whether it meets the economical and physical criteria is not addressed in this work. The following norm is proposed to measure the uniformity of deposition, and it will be used to compare the effects of different parameters on the system.

$$\|\cdot\| = \frac{1}{L}\int_0^L \left[1 - j_d/\overline{j_d}\right]^2 dy \qquad (54)$$

where j_d is the sum of the silyl and silylene fluxes at the cathode/anode and $\overline{j_d}$ is the averaged value. It's obvious that the smaller the norm, the better the uniformity.

A. Results of glow discharge

The glow discharge reactor, as was outlined in the model description, conforms to a parallel-plate configuration and it is also consistent with some of the reactors

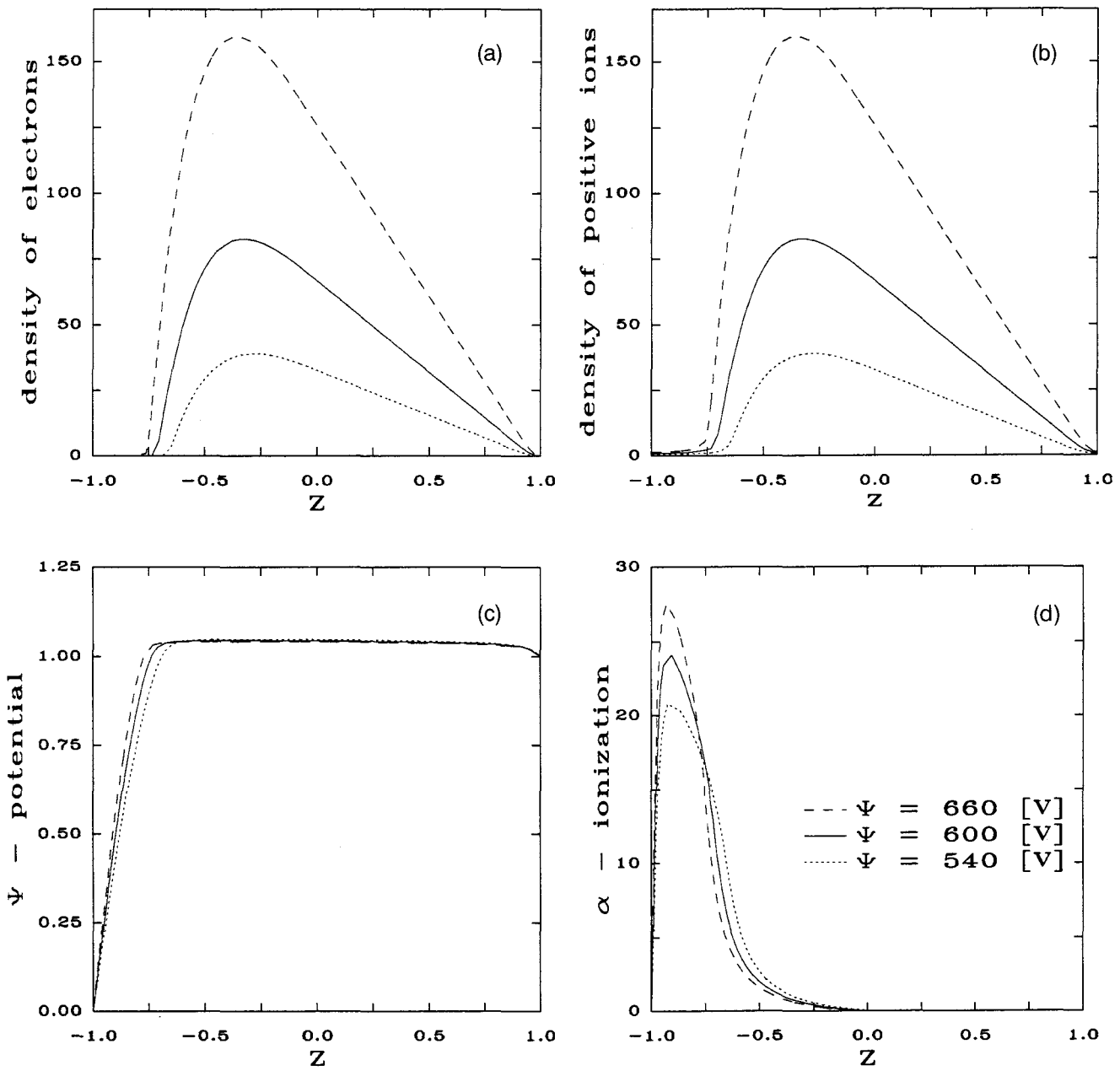

FIG. 3. Space evolution of glow discharge plasma for different voltages $V = 600, 540$, and 660 V: (a) concentration of electrons ($\times 10^{15}/m^3$), (b) concentration of positive ions ($\times 10^{15}/m^3$), (c) potential, and (d) ionization rate (1/cm).

in use at the "Sunshine Project" in Japan.[3] A base pressure of 1.5 Torr was used and the gas, containing 1% SiH_4, was fed at a rate of 10 cm/s. Figure 3 is a compounded presentation of the results for a 2 cm gap between the electrodes and for different voltages. For the base case of 600 V, the sheath thickness is approximately 14% of the gap space and it decreases to 12% when the voltage is increased by 60 V. The increase in potential decreases the width of the sheath and the electron density has increased to $164 \times 10^{15}/m^3$. In terms of reactor performance, these changes will lead to an increase in silyl deposition for the following reasons. A decrease in sheath thickness leads to a decrease in the distance silyl has to diffuse. A higher electron density, in a stronger electric field, will increase the formation of radical species. Lowering the voltage by 10% leads to a sheath thickness of $\approx$ 18% and the electron density drops to $39 \times 10^{15}/m^3$. The qualitative changes in the plasma when changing the potential are clear: increasing the potential leads to a narrower sheath and a higher electron density, electron energy increases, and silyl production goes up.

The maximum number densities of the charged species quadrupled from the lower to the higher voltage.

The potential shows little change, but a slight shift in the sheath region is noticeable. The potential increases sharply across the sheath, and is quite flat in the plasma region. A small drop in potential is noticeable near the anode. The markedly different electric field near the cathode compared to the anode will lead to quite an intense ion bombardment at the cathode and to a much lesser extent at the anode. The film's quality is influenced by the ion bombardment and a higher density film can be expected on the cathode. The ionization rate is limited to the sheath region, and the maximum increases with increased voltage, as expected. Figure 4 shows the results for 600 V, but ±10% changes in pressure. The system shows less sensitivity to these changes; e.g., the maximum number densities changed ≈80% between the extrema. Similar results are obtained when the gap distance is changed. The reader is cautioned in interpreting the results in Fig. 5 since the gap space was nondimensionalized by different values of H. The discharge exhibits even lesser sensitivity than in the previous two cases. Finally, Fig. 6 shows results for different mean temperatures in the gap. Apart from changing the density, temperature also affects the parameters in the Friedland formulation and the transport parameters (cf. Appendix). An important point that stays in neglect is the temperature dependency of the secondary emission coefficient. Also note that any thermionic emission is not considered in this model.

B. Plasma chemistry results

To solve for the concentration fields, one requires knowledge of the kinetics for SiH_4 dissociation. A full section is dedicated to this problem, because it is the part of the system one has to understand, and has to control, if one really wants to benefit from a mathematical model. Any improvement in the system is possible only if the kinetics of the dissociation reaction is improved. Tracking back this line of reasoning, it follows that the EEDF plays a very important role. The EEDF is an output of the glow discharge and it can be controlled by changing the potential and pressure (these are the most convenient control variables).

In Figs. 7–12 isolines of the molar fractions are shown for SiH_4, SiH_3, SiH_2, Si_2H_6, H_2, and H, respectively. Silane depletion is highest near the cathode, as can also be observed from the maxima in silyl and silylene concentrations in this region. The high diffusivities of the radical species lead to their presence well outside the reactor zone. However, there is a significant difference in the distribution of silyl and silylene. The latter species is also depleted by an insertion reaction with silane and thus silylene is located only near the cathode (where silane is least) while silyl is also present near the anode. The high mobilities of molecular and atomic hydrogen are reflected in the relatively large concentrations outside the reactor zone, both up and downstream. The flux of silyl and silylene to the cathode and anode can now be determined ($j_i, i = SiH_3, SiH_2$):

$$j_i = CD_i\left(\frac{dx_i}{dx} + \alpha_i x_i \frac{d\ln(T)}{dx}\right). \tag{55}$$

The rate of deposition is calculated in the same way as Yamaguchi *et al.*[23] It is expressed in unit of μm/h.

$$R_d = \frac{S}{\rho}[j_{SiH_3} + j_{SiH_2}] \times 3.6 \times 10^9, \tag{56}$$

and $\rho = 4.29 \times 10^{28}$. The sticking coefficient is taken as $S = 1$. In the following section, deposition rates and profiles are shown at different operating conditions and for different electron energy distributions.

C. Deposition

To analyze the importance of the electron energy distribution, we used the following two distributions:

$$\mathrm{EEDF}_{\mathrm{Mwel}} = \frac{4}{\pi^{0.5}} \times \frac{\epsilon}{1.128^2\bar{\epsilon}^2} e^{-\epsilon/1.128^2\bar{\epsilon}} \tag{57}$$

$$\mathrm{EEDF}_{\mathrm{Druyv}} = \frac{1.04\epsilon^{0.5}}{\bar{\epsilon}^{1.5}} e^{-0.55(\epsilon/\bar{\epsilon})^2} \tag{58}$$

In Figs. 13(a) and 13(b) the deposition profiles at the cathode are shown for the Maxwell and Druyvesteyn distributions. The rest of the conditions are consistent with the base case. The mean rate drops from 7.36 μm/h for the Maxwell distribution to 5.76 μm/h for the Druyvesteyn distribution. In both cases, silyl is the dominant depositing species. The results for the anode are shown in Figs. 14(a) and 14(b). Note the absence of silylene in this case. The mean rate now drops from 0.88 μm/h for the Maxwell distribution to 0.57 μm/h for the Druyvesteyn distribution.

The effects of branching ratios are presented in Figs. 13(a), 13(c), and 13(d) and Figs. 14(a), 14(c), and 14(d) for the cathode and anode, respectively, and also in Table II and Table III. Increasing β leads to an increase in deposition rate on both electrodes in the order of 0.3–0.5 μm/h, and the same effect holds for an increase in α. Another interesting result is the presence of a local maximum in the deposition profiles on the cathode, but the profiles on the anode are monotone. Referring to Fig. 8 the contours are converging along the channel, while they are slightly diverging near the cathode; this explains the difference in the deposition profiles.

In Fig. 15 and Fig. 16 we present the deposition profiles on the cathode and the anode, respectively, for different parameters. For the cathode in particular, the applied voltage proves to be the most sensitive parameter, and ±10% changes in the base value results

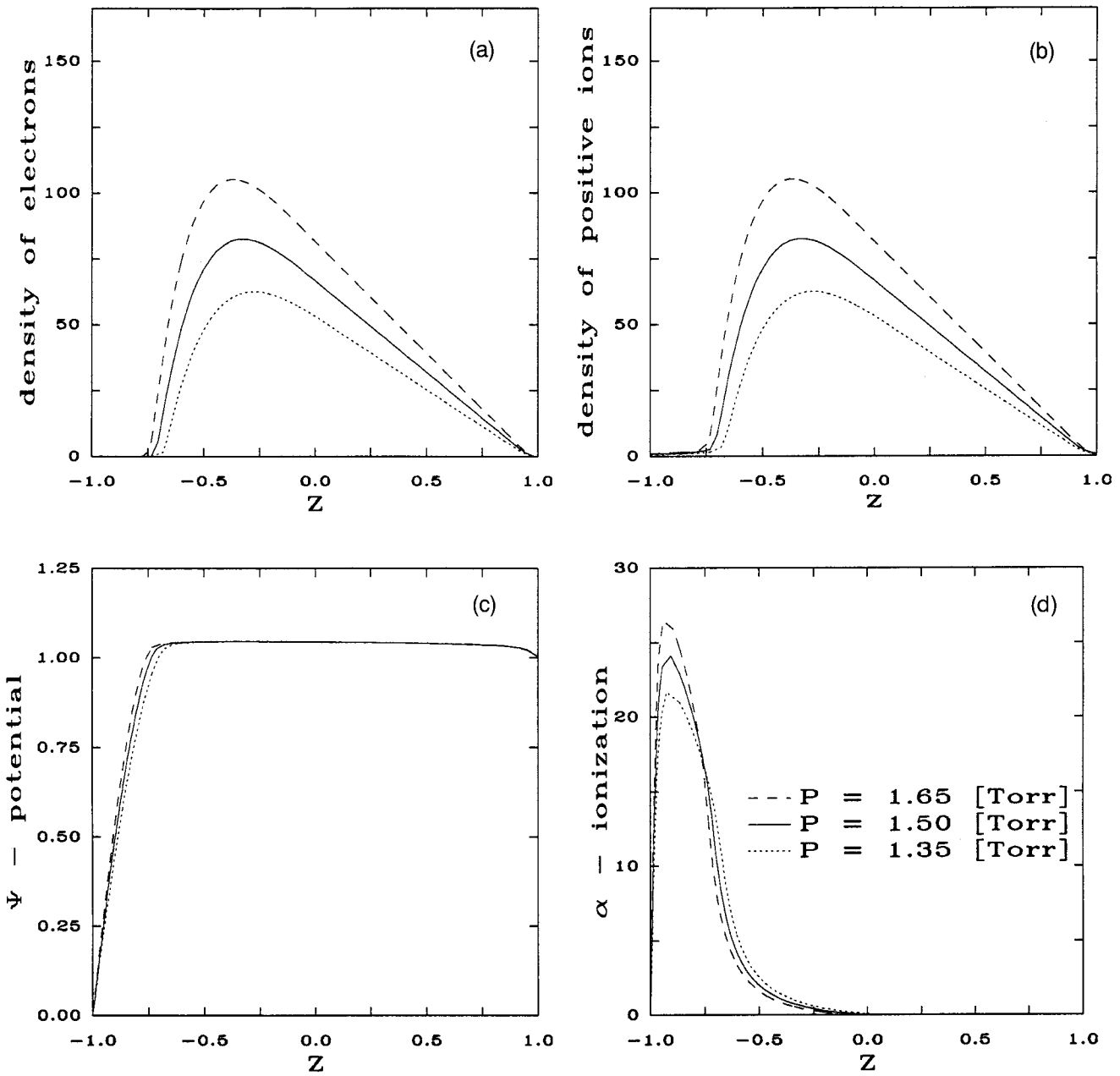

FIG. 4. Space evolution of glow discharge plasma for different pressures $P = 1.5, 1.35$, and 1.65 Torr: (a) concentration of electrons, (b) concentration of positive ions, (c) potential, and (d) ionization rate.

in +22% and −28% changes in the mean deposition rates. Similar changes in the gap distance led to 2.7% increase and 8.5% decrease in the mean rates for a smaller and larger gap, respectively. Decreasing the pressure by 10% reduced the mean rate by 11% and increasing it by 10% led to an increase of 2%. The results for the anode are also tabulated in Table III.

Temperature plays an important role as well. It affects the discharge, as was illustrated in Fig. 6, fluid flow, density of the gas, the transport properties, and the Soret effect, and these factors interact in a nonlinear way in the system. Results are shown in Fig. 15(d) and Fig. 16(d). There are two cases where the anode temperature is higher than the cathode temperature; in one case the mean temperature is more than the base value and in the other case it is below the base value. However, in both cases the deposition rate on the cathode is higher than the base case. This leads one to believe that the temperature gradient must play a role in transport of radical species. But the perplexing point is that the deposition rate on the anode also increased for the case when the anode temperature was higher than the base value. The only explanation is that the temperature has a highly nonlinear effect on the system performance.

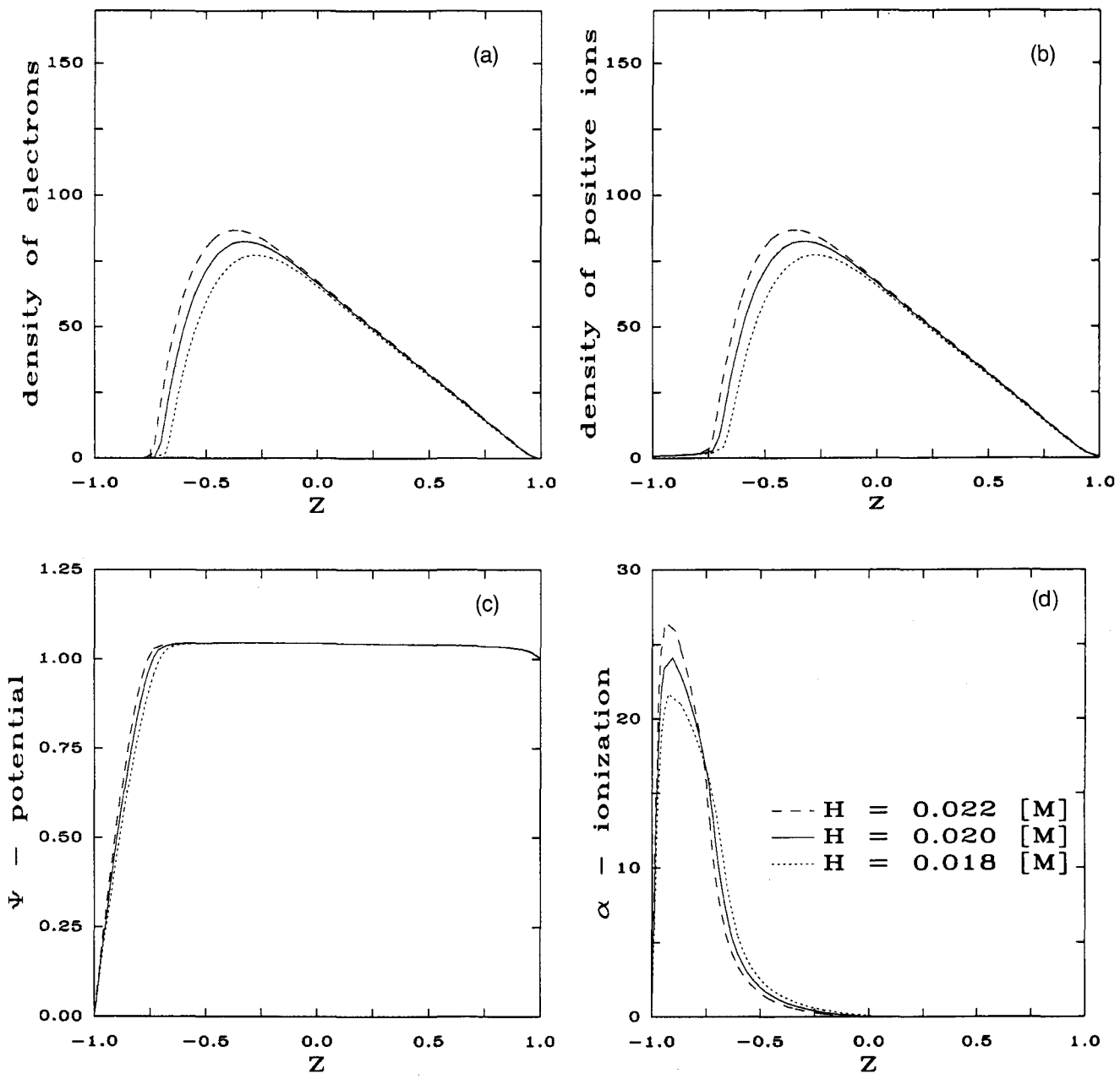

FIG. 5. Space evolution of glow discharge plasma for different gaps $H = 0.022, 0.02$, and 0.018 m: (a) concentration of electrons, (b) concentration of positive ions, (c) potential, and (d) ionization rate.

The results of the parameter sensitivity study are summarized in Table II and Table III. The sensitivity results of the measure of uniformity of the deposition are also listed in the tables. The Druyvesteyn distribution had a slightly better uniformity, but the most important factor that influences it is the length of the substrate; this is a quite logical result, but it is still useful to quantify the sensitivity of this factor. What is more interesting is the increase in uniformity with increase in gap distance and applied voltage, with the opposite holding true when these values are reduced. The uniformity is less sensitive toward pressure and electrode temperatures; also the branching ratios have less effect on the uniformity. Again we want to point out that the system is nonlinear and extrapolation of tendencies beyond the range of parameter values which were investigated is indeed not wise.

D. Design considerations

Although much empirical knowledge has been collected for the control of PECVD reactors, there exists the need for systematic design principles to design and control the reactors. An interesting approach is discussed by Tichibana[25] for an rf plasma, and they stress the

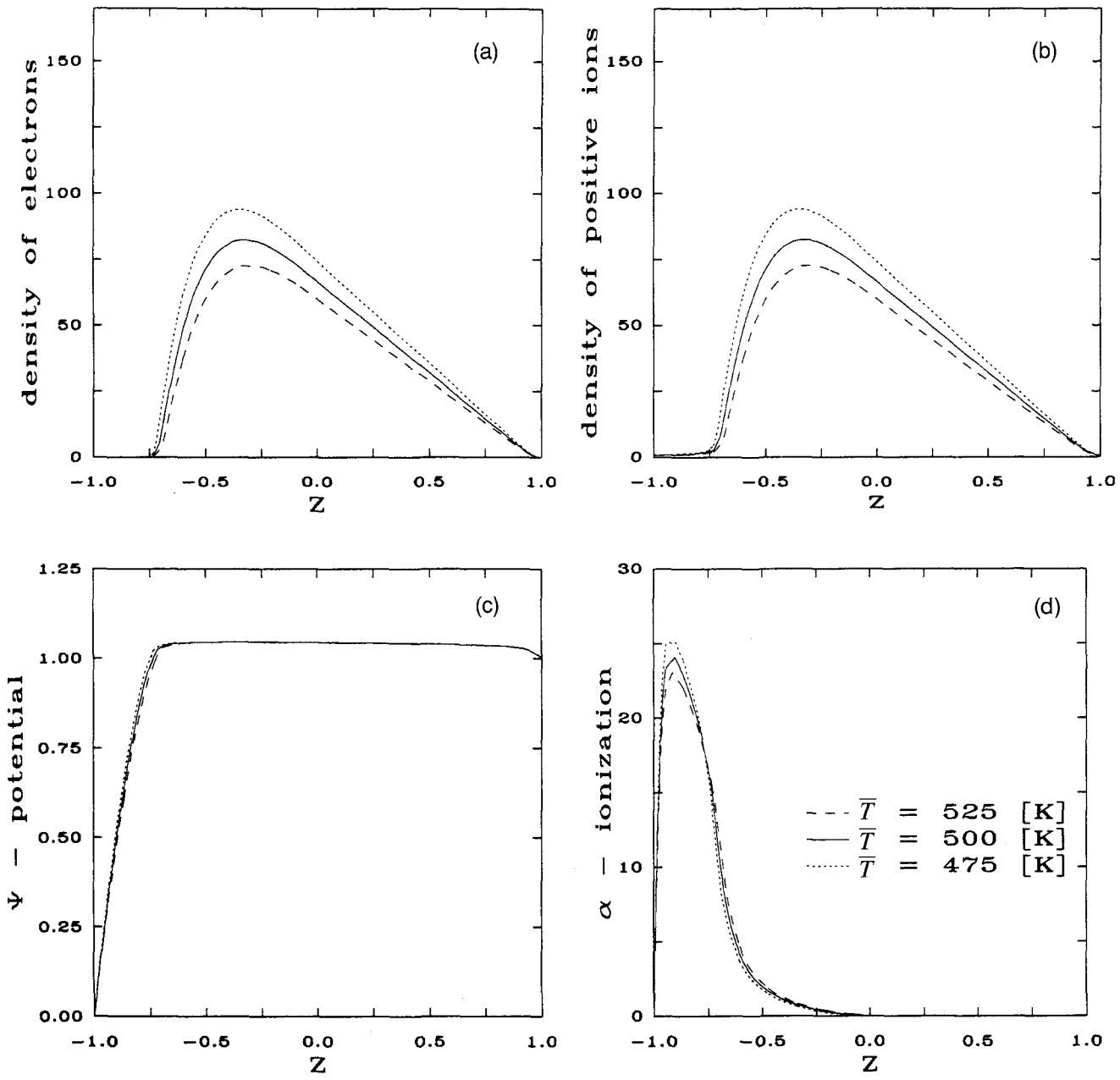

FIG. 6. Space evolution of glow discharge plasma for different gas temperatures in the reactor $\overline{T}$ = 500, 475, and 525 K: (a) concentration of electrons, (b) concentration of positive ions, (c) potential, and (d) ionization rate.

importance of controlling the energy and density of the electrons in the first place.

Increasing E/p (higher voltage, lower pressure) and increasing the mean free path for electrons will lead to an increase in the high energy tail of the EEDF, and consequently in the production of radicals. The EEDF can also be altered by changing the composition of the gas. However, the collision cross section for different species depends nonlinearly on the energy of the electrons and the outcome is not always predictable.

The radical concentrations can also be changed by the introduction of radical scavengers (such as NO), while the addition of hydrogen in Ar glow discharges lowers the mean electron energy. In chlorosilane plasmas this quenching effect of hydrogen inhibits the electron impact dissociation of $SiCl_4$, increasing the free radical concentration in the plasma. It was experimentally observed that hydrogen addition can lead to one order of magnitude increase in free radicals. The relative weight for the radical-neutral reactions can be controlled by changing the free mean path for radicals and the residence time in the reactor. Flow speed, reactor length, and pressure are the relevant control and design variables. Control of the extraction rates for neutral radicals

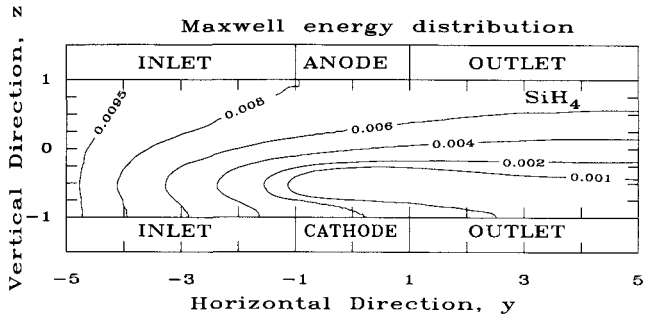

FIG. 7. Isolines of SiH_4 molar fraction in the reactor.

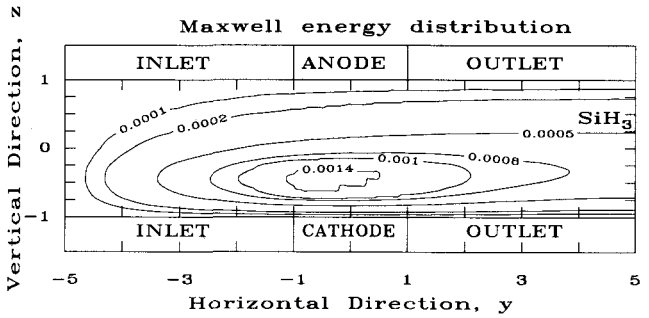

FIG. 8. Isolines of SiH_3 molar fraction in the reactor.

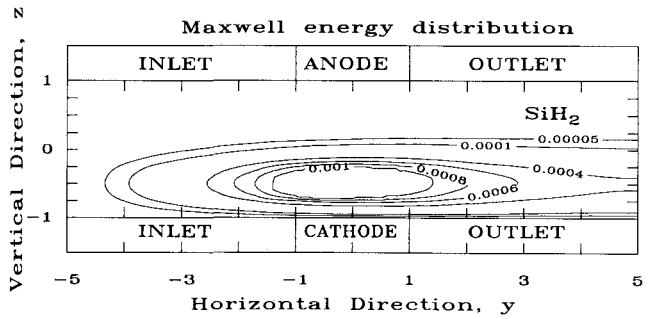

FIG. 9. Isolines of SiH_2 molar fraction in the reactor.

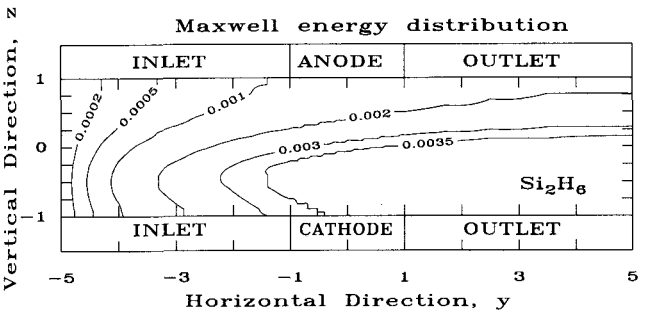

FIG. 10. Isolines of Si_2H_6 molar fraction in the reactor.

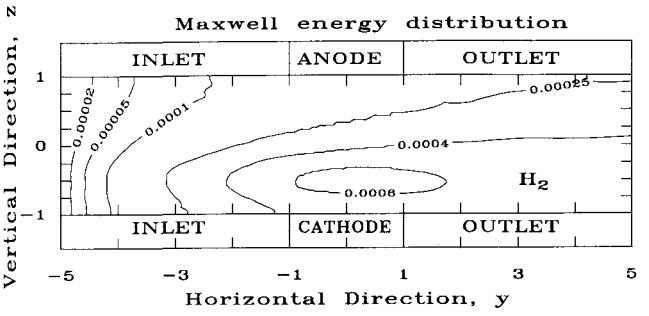

FIG. 11. Isolines of H_2 molar fraction in the reactor.

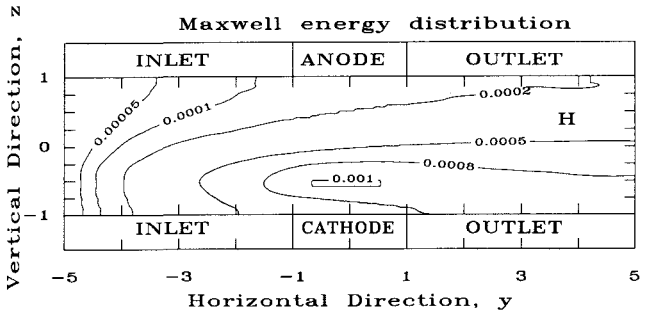

FIG. 12. Isolines of H molar fraction in the reactor.

is possible through the modification of their spatial distributions.

External deposition is becoming increasingly important, especially for applications that are sensitive toward ion bombardment. One approach is to inject the molecular gas (e.g., SiH_4) into the after section and to place the substrate at the end of the after section. Enhanced deposition can be obtained in a stagnation point flow configuration.

Another important factor is the ion bombardment of the substrate surface. Film properties are modified by the ion bombardment. Ion-neutral interactions near the cathode can significantly influence this bombardment. Charge exchange will lead to a decrease in the energy of the bombarding ions, but it can be quantified only by adapting the present model.

NOMENCLATURE

a	Ionization collision efficiency ($V^{-1} \cdot m^{-1} \cdot Torr^{-1}$)
b	Dimensionless parameter; see Table I
C	Concentration of feed gas (mole $\cdot$ m^{-3})
C_p	Specific heat capacity ($J \cdot kg^{-1} \cdot K^{-1}$)
D_i	Diffusion coefficient of i'th species ($m^2 \cdot s^{-1}$)
E	Electric field ($V \cdot m^{-1}$)
e	Unit charge (Coulomb)
$EEDF_i$	Electron energy distribution function, i = Maxwell, Druyvesteyn
Fo	Fourier number
$\mathbf{g}$	Gravity constant ($m \cdot s^{-2}$)
H	Gap space between electrodes (m)

j_i	Flux of i'th species ($m^2 \cdot s^{-1}$)
k	Total inelastic collision efficiency ($V^{-1} \cdot m^{-1} \cdot Torr^{-1}$)
$\mathbf{k}$	Conductivity tensor ($W \cdot m^{-1} \cdot K^{-1}$)
k_B	Boltzmann constant, 8.61727×10^{-5} ($eV \cdot deg^{-1}$)
k_D	Rate constant for silane dissociation (s^{-1})
k_i	Reaction rate constant ($m^3 \cdot s^{-1}$)
l_D	Debye length (Å)
n_i	Number density of i'th species (m^{-3})
N	Total number of molecules
p	Pressure in the system (Torr)
Pe_i	Peclet number of i'th species
R_g	Universal gas constant ($J \cdot mole^{-1} \cdot K^{-1}$)
Ra	Raleigh number; see Table I
R_d	Rate of deposition ($\mu m \cdot h^{-1}$)
T	Temperature of neutral and positive ions (K)
T_e	Electron temperature (eV) or (K)
t	Time (s)
$\mathbf{U}$	Velocity vector of neutral species ($m \cdot s^{-1}$)
V	Potential (V)
x_i	Mole fraction of i'th species
y	Space variable, along length of reactor (m)
z	Space variable, between electrodes (m)

Greek symbols

α	Townsend primary ionization coefficient (m^{-1})
α_i	Thermal diffusion coefficient of i'th species
β	Dimensionless parameter; see Table I
δ	Dimensionless parameter; see Table I
ϵ	Dimensionless parameter; see Table I, also used as electron energy (eV)
ϵ_0	Permittivity of free space, 8.85×10^{-12} ($C \cdot V^{-1} \cdot m^{-1}$)
ρ	Density of gas phase ($kg \cdot m^{-3}$)
μ	Viscosity of neutral species ($Pa \cdot s$)
μ_i	Mobility of i'th species ($m^2 \cdot V^{-1} \cdot s^{-1}$)
ξ	Energy, for activation or ionization (eV)
σ_i	Collision cross section for i'th process (m^2)

Subscripts

an	Anode
cat	Cathode
D	Dissociation
e	Electron
p	Positive ion
ref	Reference value

REFERENCES

1. A. Inspektor-Koren, Surf. and Coat. Technol. **33**, 31 (1987).
2. J. D. Joannopoulos and G. Lucovsky, *The physics of Hydrogenated Amorphous Silicon I* (Springer-Verlag, Berlin, 1984).
3. S. Nonaka, Jpn. J. Appl. Phys. **29**, 571 (1990).
4. J. M. Thomas, *Properties of Amorphous Silicon* (INSPEC, New York, 1985).
5. M. J. Kushner, J. Appl. Phys. **62**, 2803 (1987).
6. D. Graves and K. F. Jensen, IEEE Trans. Plasma Sci. **PS-14**, 78 (1986).
7. P. Segur, M. Yousfi, J-P. Boeuf, E. Marode, A. J. Davies, and J. G. Evans, Microscopic Treatment of non-Equilibrium Regions, Proc. 11th Conf. on Plasma (1982).
8. L. Friedland, J. Phys. D: Appl. Phys. **7**, 2246 (1974).
9. L. Friedland and Yu M. Kagan, J. Phys. D: Appl. Phys. **19**, 1019 (1986).
10. J. Vicek, J. Phys. D: Appl Phys. **22**, 623 (1988).
11. A. L. Ward, J. Appl. Phys. **33**, 2789 (1962).
12. J. J. Lowke and D. K. Davies, J. Appl. Phys. **48**, 4991 (1977).
13. M. J. Kushner, J. Appl. Phys. **63** (8), 2532 (1988).
14. J-P. Boeuf, J. Appl. Phys. **63** (1988).
15. K. P. Traar, W. Mader, O. Heinreichsberger, and S. Selberherr, in *Supercomputing 90* (IEEE Comp. Press).
16. P. M. Gresho, R. L. Lee, and R. L. Sani, in *Recent Advances in Numerical Methods, Fluids*, edited by C. Taylor and K. Morgan (Pineridge Press, Swansea), Vol. 1, pp. 22–79.
17. T. J. R. Hughes and A. N. Brooks, in *Finite Element Methods for Convective Dominated Flows* (AMD 34, ASME, New York, 1979).
18. A. N. Brooks and T. J. R. Hughes, Comp. Meth. Mech., 32 (1982).
19. P. M. Martineau and P. B. Davies, Chem. Brit. Oct., 1018 (1989).
20. J. M. Thomas, in *Properties of Amorphous Silicon* (INSPEC New York, 1985).
21. N. Itabashi, N. Nishiwaki, M. Magane, S. Naito, T. Goto, A. Matsuda, C. Yamada, and E. Hirota, Jpn. J. Appl. Phys. **29**, L505 (1990).
22. J. Perrin, J. P. M. Schmitt, G. DeRosny, B. Drevillon, J. Huc, and A. Lloret, Chem. Phys. **73**, 383 (1982).
23. Y. Yamaguchi, A. Sumiyama, R. Hattori, Y. Morokuma, and T. Makabe, J. Phys. D: Appl. Phys. **22**, 505 (1989).
24. Y. Ohmori, M. Shimozuma, and H. Tagashira, J. Phys. D: Appl. Phys. **19**, 1029 (1986).
25. K. Tichibana, Pure and Appl. Chem. **60**, 769 (1988).
26. E. W. McDaniel and E. A. Mason, *The Mobility and Diffusion of Ions in Gases* (John Wiley and Sons, New York, 1973).
27. S-K. Park and D. J. Economou, J. Appl. Phys. **68**, 3904 (1990).
28. A. A. Kruithof and F. M. Penning, Physica **4**, 430 (1937).
29. M. Suzuki, T. Taniguchi, and H. Tagashira, J. Phys. D: Appl. Phys. **23**, 842 (1990).
30. H. Itoh, M. Kawaguchi, M. Takada, Y. Nakao, and H. Tagashira, J. Phys. D: Appl. Phys. **22**, 1095 (1989).
31. R. J. Carman, J. Phys. D: Appl. Phys. **22**, 55 (1989).

APPENDIX: PHYSICAL PROPERTIES

The correctness of a modeling effort is determined to a large extent by the accuracy and availability of reliable physical data. The physical properties of the glow discharge are first discussed and then the properties that are required in the hydrodynamic model are presented. Complete references to the source of the data are given. When the property was determined by a correlation, the method is briefly outlined.

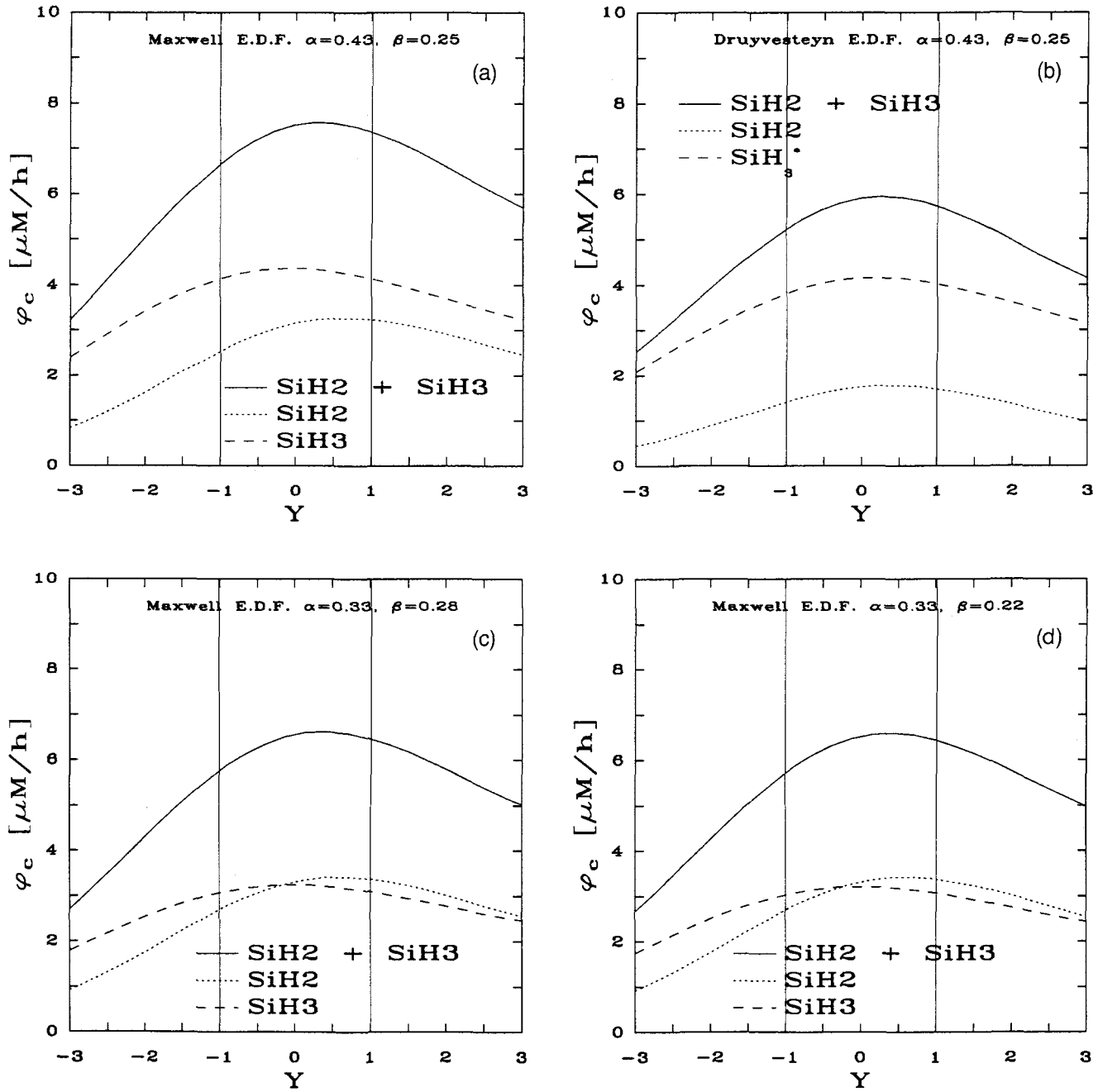

FIG. 13. Contribution of different radicals to total deposition rate along the cathode for different electron distribution functions and different branching ratios. (a) Maxwell electron distribution function; $\alpha = 0.43$ and $\beta = 0.25$. (b) Druyvesteyn electron energy distribution function; $\alpha = 0.43$ and $\beta = 0.25$. (c) Maxwell electron distribution function; $\alpha = 0.33$ and $\beta = 0.28$. (d) Maxwell electron distribution function; $\alpha = 0.33$ and $\beta = 0.22$.

A. Glow discharge properties

The Ar discharge was considered in this study; i.e., the participation of SiH_4 toward the formation of charged species was seen as negligible. According to the governing Eqs. (3)–(6) the following parameters determine the physical property of the discharge: (i) electron diffusion and mobility, D_e and μ_e; (ii) ion diffusion and mobility, D_p and μ_p; (iii) total inelastic and ionization collision efficiencies, k and a; and (iv) secondary electron emission coefficient, γ.

The operation of the discharge covers the 'rough vacuum' 0.1–10 Torr and the temperature range 600–650 K. Temperature and pressure dependencies of the parameters are reported where relevant, but the dependencies of mobilities and diffusion on the electric field were not considered.

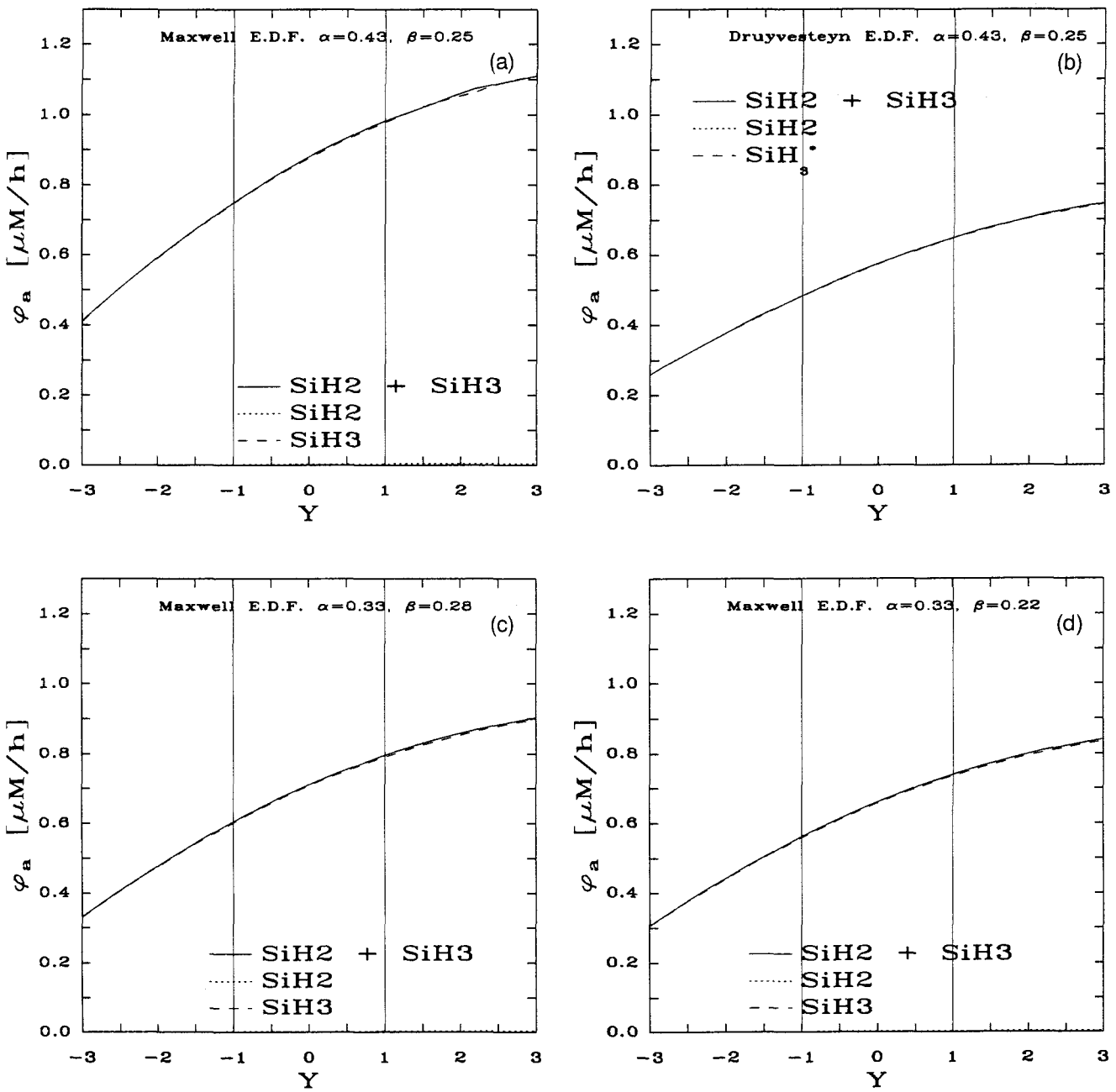

FIG. 14. Contribution of different radicals to total deposition rate along the anode for different electron distribution functions and different branching ratios. (a) Maxwell electron distribution function; $\alpha = 0.43$ and $\beta = 0.25$. (b) Druyvesteyn electron energy distribution function; $\alpha = 0.43$ and $\beta = 0.25$. (c) Maxwell electron distribution function; $\alpha = 0.33$ and $\beta = 0.28$. (d) Maxwell electron distribution function; $\alpha = 0.33$ and $\beta = 0.22$.

In Table IV the properties are listed for $p = 1$ Torr and $T = 600$ K.

Note that the excitation energy is the average energy of excitation from the ground level to $4s[3/2]_2$ and $4s[3/2]_1$.

The electron diffusion and mobilities depend on the electric field; however, we considered these coefficients as constant for our model and to be consistent with the theory developed by Friedland,[8] we used average values at high $E/p \approx O(100)$. The N in Table IV denotes the total number density:

$$N = 9.657 \times 10^{18} \frac{p}{T} \quad (\text{cm}^{-3}) \tag{59}$$

where p is the total pressure in Torr and T denotes the gas temperature (K). At high E/p (McDaniel and Mason,[26] Fig. 7-1-C-1) the reduced mobility is

$$\mu_{pr} = 1 \tag{60}$$

$$= \frac{273.16p}{760T}\mu_p \tag{61}$$

TABLE II. Parametric study of PECVD, cathode.

No.	H (m)	L (m)	P_0 (Torr)	T_a (K)	T_c (K)	Ψ (V)	v_f (m/s)	x_{Sih_4}	ψ (μm/h)	Norm
1[a]	0.02	0.2	1.5	500	500	600	0.1	0.01	7.36	$1.18 \cdot 10^{-3}$
2[b]	0.02	0.2	1.5	500	500	600	0.1	0.01	5.76	$1.13 \cdot 10^{-3}$
3	0.02	0.2	1.5	500	500	660	0.1	0.01	8.99	$8.94 \cdot 10^{-3}$
4	0.02	0.2	1.5	500	500	540	0.1	0.01	5.29	$1.64 \cdot 10^{-3}$
5	0.022	0.2	1.5	500	500	600	0.1	0.01	6.72	$8.98 \cdot 10^{-3}$
6	0.018	0.2	1.5	500	500	600	0.1	0.01	7.55	$2.06 \cdot 10^{-3}$
7	0.02	0.2	1.65	500	500	600	0.1	0.01	7.50	$1.03 \cdot 10^{-3}$
8	0.02	0.2	1.35	500	500	600	0.1	0.01	6.55	$1.60 \cdot 10^{-3}$
9	0.02	0.22	1.5	500	500	600	0.1	0.01	7.84	$2.07 \cdot 10^{-3}$
10	0.02	0.18	1.5	500	500	600	0.1	0.01	6.78	$7.45 \cdot 10^{-4}$
11	0.02	0.2	1.5	550	500	600	0.1	0.01	8.79	$1.24 \cdot 10^{-3}$
12	0.02	0.2	1.5	450	500	600	0.1	0.01	5.81	$1.15 \cdot 10^{-3}$
13	0.02	0.2	1.5	500	550	600	0.1	0.01	6.23	$1.43 \cdot 10^{-3}$
14	0.02	0.2	1.5	500	450	600	0.1	0.01	8.62	$9.74 \cdot 10^{-3}$
15	0.02	0.2	1.5	500	500	600	0.11	0.01	7.36	$1.18 \cdot 10^{-3}$
16	0.02	0.2	1.5	500	500	600	0.09	0.01	7.36	$1.18 \cdot 10^{-3}$
17	0.02	0.2	1.5	500	500	600	0.1	0.011	7.80	$1.20 \cdot 10^{-3}$
18	0.02	0.2	1.5	500	500	600	0.1	0.009	6.88	$1.16 \cdot 10^{-3}$
19[c]	0.02	0.2	1.5	500	500	600	0.1	0.01	6.86	$1.18 \cdot 10^{-3}$
20[d]	0.02	0.2	1.5	500	500	600	0.1	0.01	6.41	$1.43 \cdot 10^{-3}$
21[e]	0.02	0.2	1.5	500	500	600	0.1	0.01	6.38	$1.47 \cdot 10^{-3}$

TABLE III. Parametric study of PECVD, anode.

No.	H (m)	L (m)	P_0 (Torr)	T_a (K)	T_c (K)	Ψ (V)	v_f (m/s)	x_{Sih_4}	ψ (μm/h)	Norm
1[a]	0.02	0.2	1.5	500	500	600	0.1	0.01	0.88	$5.96 \cdot 10^{-3}$
2[b]	0.02	0.2	1.5	500	500	600	0.1	0.01	0.57	$6.95 \cdot 10^{-3}$
3	0.02	0.2	1.5	500	500	660	0.1	0.01	0.90	$5.84 \cdot 10^{-3}$
4	0.02	0.2	1.5	500	500	540	0.1	0.01	0.86	$6.02 \cdot 10^{-3}$
5	0.022	0.2	1.5	500	500	600	0.1	0.01	0.82	$5.28 \cdot 10^{-3}$
6	0.018	0.2	1.5	500	500	600	0.1	0.01	0.96	$6.59 \cdot 10^{-3}$
7	0.02	0.2	1.65	500	500	600	0.1	0.01	0.84	$6.00 \cdot 10^{-3}$
8	0.02	0.2	1.35	500	500	600	0.1	0.01	0.93	$5.91 \cdot 10^{-3}$
9	0.02	0.22	1.5	500	500	600	0.1	0.01	0.75	$8.13 \cdot 10^{-3}$
10	0.02	0.18	1.5	500	500	600	0.1	0.01	0.97	$3.69 \cdot 10^{-3}$
11	0.02	0.2	1.5	550	500	600	0.1	0.01	0.97	$5.95 \cdot 10^{-3}$
12	0.02	0.2	1.5	450	500	600	0.1	0.01	0.79	$5.98 \cdot 10^{-3}$
13	0.02	0.2	1.5	500	550	600	0.1	0.01	0.88	$5.99 \cdot 10^{-3}$
14	0.02	0.2	1.5	500	450	600	0.1	0.01	0.87	$5.91 \cdot 10^{-3}$
15	0.02	0.2	1.5	500	500	600	0.11	0.01	0.88	$5.96 \cdot 10^{-3}$
16	0.02	0.2	1.5	500	500	600	0.09	0.01	0.88	$5.96 \cdot 10^{-3}$
17	0.02	0.2	1.5	500	500	600	0.1	0.011	0.97	$5.89 \cdot 10^{-3}$
18	0.02	0.2	1.5	500	500	600	0.1	0.009	0.78	$6.04 \cdot 10^{-3}$
19[c]	0.02	0.2	1.5	500	500	600	0.1	0.01	0.74	$6.07 \cdot 10^{-3}$
20[d]	0.02	0.2	1.5	500	500	600	0.1	0.01	0.71	$6.07 \cdot 10^{-3}$
21[e]	0.02	0.2	1.5	500	500	600	0.1	0.01	0.66	$6.13 \cdot 10^{-3}$

[a]Reference case: Maxwell energy distribution; branching ratios: $\alpha = 3/7$ and $\beta = 12/49$.
[b]Druyvesteyn energy distribution; branching ratios: $\alpha = 3/7$ and $\beta = 12/49$.
[c]Maxwell energy distribution; branching ratios: $\alpha = 3/7$ and $\beta = 4/21$.
[d]Maxwell energy distribution; branching ratios: $\alpha = 1/3$ and $\beta = 2/7$.
[e]Maxwell energy distribution; branching ratios: $\alpha = 1/3$ and $\beta = 2/9$.

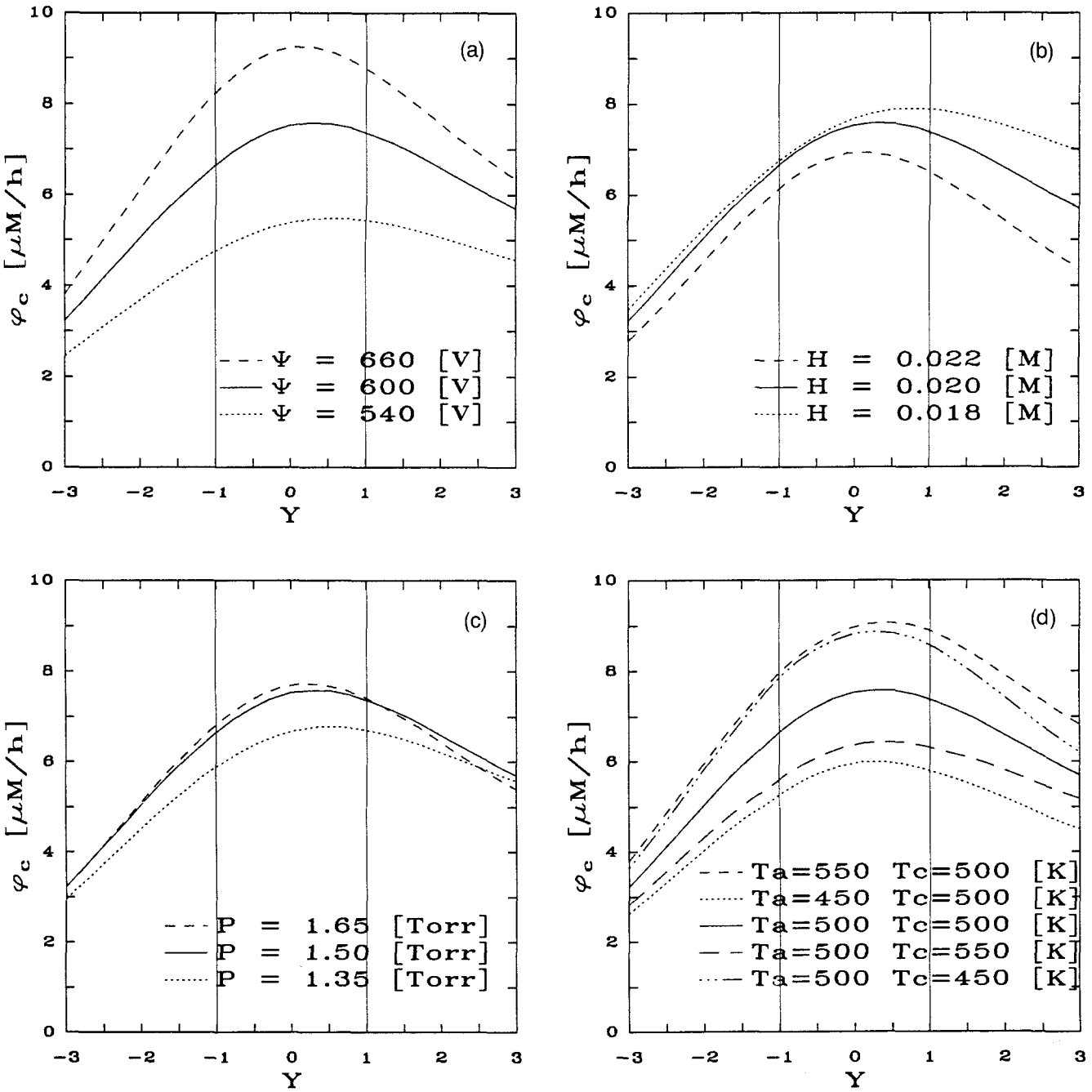

FIG. 15. Deposition rates along the cathode for different parameters. (a) Effect of different voltages, $V = 660, 600$, and 540 V. (b) Effect of different gaps, $H = 0.022, 0.02$, and 0.018 m. (c) Effect of different pressures, $P = 1.65, 1.5$, and 1.35 Torr. (d) Effect of different temperatures on the anode and on the cathode; $T_a = 550$ K and $T_c = 500$ K, $T_a = 450$ K and $T_c = 500$ K, $T_a = 500$ K and $T_c = 500$ K, $T_a = 500$ K and $T_c = 550$ K, and $T_a = 500$ K and $T_c = 450$ K.

Hence,

$$\mu_p = \frac{760T}{273.16p} \quad (\mathrm{cm^2\ V^{-1}\ s^{-1}}) \tag{62}$$

and the reduced mobility will be assumed to be constant for the range of operating conditions that are considered. The diffusion coefficient D_p depends on gas temperature. The temperature dependence of the zero-field mobility K_0 for Ar^+ in Ar was reported in McDaniel and Mason[26] (p. 311). We fitted a linear curve through their data and obtained

$$K_0 = -\frac{T}{450} + \frac{7}{3} \tag{63}$$

The diffusion coefficient is then obtained from

$$D_p = \frac{T^2 K_0}{4172p} \quad (\mathrm{cm^2 \cdot s^{-1}}) \tag{64}$$

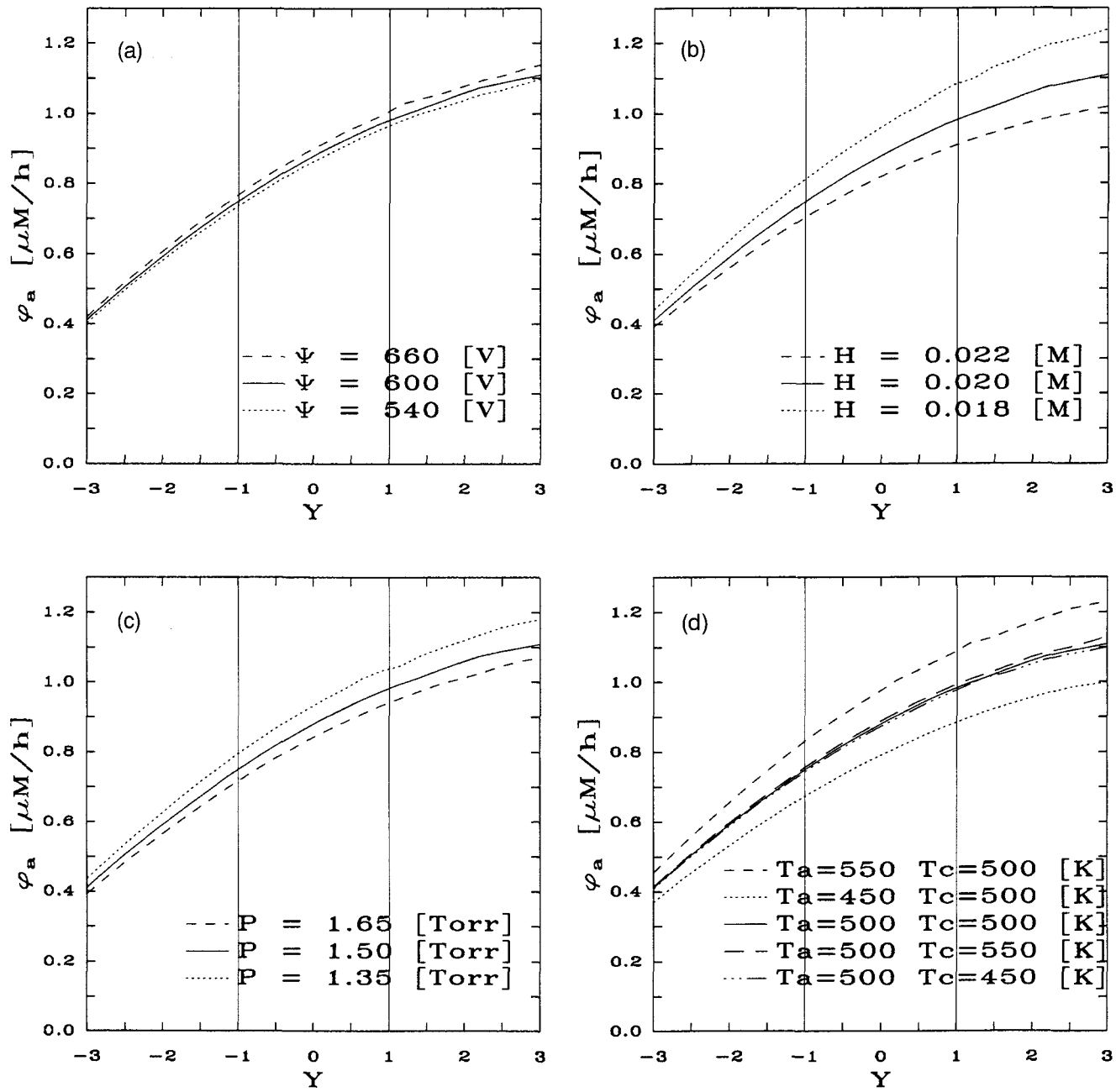

FIG. 16. Deposition rates along the anode for different parameters. (a) Effect of different voltages, $V = 660, 600$, and 540 V. (b) Effect of different gaps, $H = 0.022, 0.02$, and 0.018 m. (c) Effect of different pressures, $P = 1.65, 1.5$, and 1.35 Torr. (d) Effect of different temperatures on the anode and on the cathode; $T_a = 550$ K and $T_c = 500$ K, $T_a = 450$ K and $T_c = 500$ K, $T_a = 500$ K and $T_c = 500$ K, $T_a = 500$ K and $T_c = 550$ K, and $T_a = 500$ K and $T_c = 450$ K.

These values can be compared to the values used by Park and Economou[27] for an Ar-like plasma, which were reported at a gas temperature of 273 K.

The total inelastic and ionization collision efficiencies are determined from the local-equilibrium form of the Friedland equation. If local-equilibrium holds, plots of α/p vs $(E/p)^{1/2}$ at large values of E/p is linear with slope $a^{1/2}$ and abscissae $k\xi/2$. Table IV of Kruithof and Penning,[28] listing α/E for different E/p, was used to determine a and k.

B. Physical properties for hydrodynamic model

Transport and physical properties of the Ar/SiH_4 mixture are required for the hydrodynamic model. To include the temperature dependence of the properties in the model, it is advantageous to use analytical expressions.

The Hirschfelder, Bird, Spotz formula was used to calculate the viscosities of the pure gases.

$$\mu = 2.2693 \times 10^{-6} \frac{(MT)^{1/2}}{\sigma^2 \Omega^{2,2}} \quad \text{Pa} \cdot \text{s} \qquad (65)$$

TABLE IV. Properties of glow discharges.

Property	Value	Reference
$ND_e(E)$	3.3×10^{22} cm$^{-1} \cdot$ s^{-1}	Suzuki *et al.*,[29] Itoh *et al.*[30]
$\frac{D_e}{\mu_e}(E)$	3.5 V	Suzuki *et al.*[29]
$D_p(p,T)$	86.29 cm$^2 \cdot$ s^{-1}	McDaniel and Mason[26]
$\mu_p(p,T)$	1669.35 cm$^2 \cdot$ s$^{-1} \cdot$ V^{-1}	McDaniel and Mason[26]
a	0.30(V $\cdot$ cm $\cdot$ Torr)$^{-1}$	Kruithof and Penning[28]
k	0.465(V $\cdot$ cm $\cdot$ Torr)$^{-1}$	Kruithof and Penning[28]
$\xi = \frac{1}{2}(\xi_{ion} + \xi_{ex})$	$\frac{1}{2}$(15.8 + 11.6)eV	Carman,[31] Vicek[10]
γ	0.001	Yamaguchi *et al.*[23]

M is the molecular weight, T is the temperature, and σ is a force constant defined in terms of the Lennard–Jones equation. $\Omega^{2,2}$ is a function of the variable (kT/ϵ). If experimental data were available, Sutherland's equation was used to present the temperature dependency of the gas viscosity

$$\mu = B\frac{T^{3/2}}{T + C} \tag{66}$$

where B and C are constants, characteristic for a given gas. To estimate the viscosity of a gaseous mixture, use was made of the Wilke equation

$$\mu_m = \sum_i^N \frac{\mu_i}{\sum_j \frac{x_j}{x_i}\phi_{i,j}} \tag{67}$$

μ_i is the viscosity of the i-th component and x_i is the mole fraction. $\phi_{i,j}$ is defined as follows:

$$\phi_{i,j} = \frac{\left[1 + \left(\frac{\mu_i}{\mu_j}\right)^{0.5}\left(\frac{M_j}{M_i}\right)^0 \cdot 25\right]^2}{2^{1.5}\left(1 + \frac{M_i}{M_j}\right)^{0.5}} \tag{68}$$

Thermal conductivity estimates of the gases were based on the kinetic theory for gases, taking molecular interactions into consideration. For a pure monatomic gas the Bird, Hirschfelder, Curtiss equation was used

$$\lambda = 8.3224 \times 10^{-2}\frac{(T/M)^{0.5}}{\sigma^2\Omega^{2,2}} \quad \text{W} \cdot \text{m}^{-1} \cdot \text{K}^{-1} \tag{69}$$

For a pure polyatomic gas (in our case silane and radicals) the following relation was used:

$$\lambda = 2.6689 \times 10^{-3}\frac{(T/M)^{0.5}}{\sigma^2\Omega^{2,2}} \quad (C_v + 18.702) \quad \text{W} \cdot \text{m}^{-1} \cdot \text{K}^{-1} \tag{70}$$

The thermal conductivity of a gas mixture was calculated by the Wassilica equation

$$\lambda_m = \sum_i^N \frac{\lambda_i}{\sum_j \frac{x_j}{x_i}A_{i,j}} \tag{71}$$

The values of the coefficients $A_{i,j}$ can be calculated from the Lindsay and Bromley relationship

$$A_{i,j} = 0.25\left[1. + \left(\frac{\mu_i}{\mu_j}\left(\frac{M_j}{M_i}\right)^{0.75}\frac{1 + C_i/T}{1 + C_j/T}\right)^{0.5}\right]^2 \times \frac{1 + C_{ij}/T}{1 + C_i/T} \tag{72}$$

C_i is the constant in the Sutherland equation for thermal conductivity. In addition, $C_{ij} = [C_iC_j]^{0.5}$.

Diffusion in gases is calculated from the Wilke and Lee equation

$$D_{1,2} = \frac{BT^{1.5}}{p\sigma_{1,2}^2\Omega^{1,1}}\left(\frac{m_1 + m_2}{m_1m_2}\right)^{0.5} \tag{73}$$

and the coefficient B is a function of the molecular weights of the gases

$$B = 2.14 \times 10^{-7} - 4.92 \times 10^{-8}\left(\frac{M_1 + M_2}{M_1M_2}\right)^{0.5} \tag{74}$$

Thermal diffusion is calculated from the kinematic viscosity and the thermal diffusion ratio K_{TD}

$$K_{TD} = 5(C - 1)\frac{S_1n_1 - S_2n_2}{Q_1n_1^2 + Q_2n_2^2 + Q_{12}n_1n_2}n_1n_2 \tag{75}$$

where n_1 and n_2 are the volume fractions of the components and

$$S_1 = m_1E_1 - 4Am_1m_2 - 3m_2(m_2 - m_1) \tag{76}$$

$$Q_1 = E_1(6m_2^2 + (5 - 4B)m_1^2 + 8Am_1m_2) \tag{77}$$

$$Q_{12} = 3(m_1 - m_2)^2(5 - 4B) + 4m_1m_2A(11 - 4B) + 2E_1E_2 \tag{78}$$

with relations for S_2 and Q_2 derived as for S_1 and $Q_1 \cdot m_1, m_2$, and m are defined as

$$m_1 = \frac{M_1}{M_1 + M_2} \tag{79}$$

$$m_2 = \frac{M_2}{M_1 + M_2} \tag{80}$$

$$m = m_1 - m_2 \tag{81}$$

A, B, C, E_1, and E_2 depend on the temperature and the interaction between molecules

$$A = \frac{\Omega^{2,2}}{\Omega^{1,1}} \tag{82}$$

$$B = \frac{5\Omega^{1,2}\Omega^{1,3}}{5\Omega^{1,1}} \tag{83}$$

$$C = \frac{2\Omega^{1,2}}{5\Omega^{1,1}} \tag{84}$$

$$E_1 = \frac{2\Omega^{2,2}}{5(1 - m)\Omega^{1,1}} \tag{85}$$

$$E_2 = \frac{2\Omega^{2,2}}{5(1 + m)\Omega^{1,1}} \tag{86}$$

All these relations were included in a program to calculate the properties of any ratio between Ar and SiH_4 at any pressure and temperature. The extension to include different gaseous components, e.g., N_2 or Cl_2, is straightforward.